REPORT

February 1, 1992–Januar 31, 1993

ONR Grant No. N00014-92-J-1434

Submitted to:

Dr. A. John Sedriks

(703) 696-4402

The US DEPARTMENT OF NAVY

OFFICE OF NAVAL RESEARCH

800 N. Quincy St., Arlington, VA

Entitled:

SURFACE TREATMENT OF HYDROGEN ABSORPTION INTO ALLOYS

by

Principal Investigator:

Dr. Ralph E. White and Dr. Branko N. Popov

Department of Chemical Engineering

Texas A&M University, College Station, Texas, 77840

February, 1993

I. SURFACE TREATMENT FOR MITIGATION OF HYDROGEN ABSORPTION AND PENETRATION INTO AISI 4340 STEEL

G. Zheng, B. N. Popov* and R. E. White*

Department of Chemical Engineering

University of South Carolina

Columbia, SC, 29208

Submitted as a technical paper to the Editor of

Journal of Electrochemical Society

10 South Main Street

Pennington, New Jersey 08534-2896

March, 1993

Key words: hydrogen permeation, additives, surface treatment

---

*Electrochemical Society Active Member

Abstract

The effectiveness of underpotential deposition of Zn, Bi and Pb onto 4340 steel substrates on the reduction of hydrogen evolution and on the degree of hydrogenation ingress was determined. It is shown that the underpotentially deposited Zn, Bi and Pb from their plating solutions inhibit the discharge of hydrogen. In the presence of Bi on the substrate surface, the hydrogen discharge currents are reduced drastically (by up to 20 times) compared with the value obtained on bare steel. As a consequence, the underpotentially deposited zinc, bismuth and lead on AISI 4340 steel membranes reduce the steady state hydrogen flux by 52%, 65% and 71%, respectively.

Introduction

The practical use of steel and high strength alloys is limited by cracking hazards due to hydrogen penetration and hydrogen accumulation in the bulk of these alloys (1–2). Hydrogen embrittlement occurs as a result of hydrogen absorption on the metal surface followed by diffusion into the crystalline lattice of the substrate. The irreversible accumulation of hydrogen in the bulk of the alloy leads to deterioration of its mechanical properties. In the presence of absorbed hydrogen, changes occur in both the lattice structure and the chemical composition of the alloy. Regardless of the various methods to decrease hydrogen embritlement (3–4), it is impossible to reduce the hydrogen penetration rate onto the alloy substrate to a level which provides the elimination of hydrogenation cracking hazards. A possible solution of this problem is

underpotential deposition of Zn, Bi or Pb onto the alloy which should lead to a sharp reduction in the corrosion rate and the degree of hydrogenation ingress.

Drazic and Vorkapic (5) established that the presence of metal ions (Cd^{2+}, Mn^{+} and Zn^{+2}) more electronegative than the cathodic potential for the hydrogen evolution reaction on iron in a 0.25 M H_2SO_4 solution, inhibits the hydrogen evolution reaction and corrosion of iron. This effect has been explained as the underpotential deposition of the adatoms of these metals on iron. By investigating the mechanism of electrochemical reduction of zinc, Despic et al. (6) found that in slightly acidic sulphate electrolytes, zinc ions are underpotentially deposited on gold and platinum substrates. By studying the polarization and corrosion behavior of iron in perchlorate, chloride and sulphate base electrolytes, Juttner (7) found that as a result of the underpotential adsorption of lead and thallium on iron substrate, the active iron dissolution process as well as the charge transfer controlled hydrogen evolution are inhibited drastically. The inhibition of the cathodic hydrogen evolution reaction was explained that is due to the lower binding energy of the hydrogen adatoms on Pb and Tl adsorbates (8–9). The inhibiting action of Pb^{2+} on stress corrosion cracking of austenitic stainless steels in acidic chloride media has been evaluated by Lafrancony et al. (10). It has been found that lead ions even in traces can inhibit the occurrence of stress corrosion cracking (s.c.c) due to the inhibition of the cathodic process of hydrogen evolution. Underpotential deposition of Pb^{+2} was invoked as an explanation of the inhibition of the reaction step involving the adsorption of hydrogen at the alloy surface. Cadle and Bruckenstein (11) studied the reduction of bismuth in 0.12 M perchloric acid using

ring-disc electrode. They found that the cathodic processes are the reduction of adsorbed bismuth, reduction of bismuth at underpotential, and the convective-diffusion controlled limiting wave for bismuth reduction, which produces distinct surface layers of bismuth in depths of two, three and four monolayers as well as bulk alloy and bulk bismuth. Kudryavtsev et al. (12) by comparing their results obtained by cyclic voltammetry with data derived by the Devanathan-Stachurski method under identical conditions found that the underpotential absorption of zinc onto ARMCO-iron reduces the amount of atomic hydrogen adsorbed in the substrate.

The objective of this work is to estimate the effectiveness of underpotential deposition (UPD) of Zn^{+2}, Pb^{+2} and Bi^{+3} on the reduction of the hydrogen evolution rate and the degree of hydrogenation ingress into AISI 4340 steel. The sharp reduction in corrosion rate was expected due to the kinetic limitations of the hydrogen discharge reaction on the deposited monolayers. As a consequence one can expect a decrease of the degree of the H_{ads} surface coverage to occur decreasing the hydrogen penetration rate in the alloy.

Experimental

The electrochemical cell employed for these studies was a conventional three-compartment design with contact between the working electrode compartment and the reference electrode via a Luggin probe. The polarization experiments were carried out using AISI 4340 steel rotating disc electrode with a geometric area of 0.5 cm^2. The electrode was mechanically polished to a fine finish, activated in sulfuric acid, washed

with ethanol and in doubly distilled water.

Using the Devanathan-Stachurski permeation technique (13), both the rate of hydrogen absorption and permeation through AISI 4340 steel was measured continuously as a function of time. The permeation rate through a thin membrane of the alloy was measured by setting the potential on the "diffusion side" of the membrane (the side from which the hydrogen emerges) at a value which corresponds to a practically zero concentration of absorbed atomic hydrogen on the surface (13). This condition is maintained by instantaneous ionization of all hydrogen atoms which have diffused through the membrane and have emerged on the diffusion side. The measured current is directly proportional to the hydrogen permeation rate, which can be measured conveniently with a high degree of accuracy and sensitivity. These experiments were carried out in a system with two working compartments, separated by a bipolar AISI 4340 steel membrane. The alloy membrane on the cathodic side of the cell was polarized potentiostatically, creating conditions for underpotential deposition and hydrogen evolution. The following reference electrodes were used: in the anodic compartment Hg/HgO; in the cathodic compartment $Hg/HgSO_4$ or SCE. In the anodic compartment of the cell, the steel membrane was polarized potentiostatically at –0.3 V vs Hg/HgO reference electrode and the amount of oxidized atomic hydrogen was monitored continuously using a chart recorder. The details of the permeation cell and the auxiliary equipment are given by Subramanyan (1). Prior to the permeation experiment, the steel membrane with a thickness of 0.3 mm was mechanically polished to a fine finish, saturated with hydrogen in 0.1 N H_2SO_4 by maintaining for 10 hours a cathodic

current density of 10 mA/cm^2. Then, the membrane was etched for 20 seconds in a solution containing methyl alcohol and 1% H_2SO_4, rinsed with distilled water, dried in air and fitted into the permeation cell. To avoid a possible passivation or dissolution, the anodic side of the membrane was coated with a thin layer (0.15–0.20 μm) of palladium. The deposition was carried out in electrolyte containing $2x10^{-5}$ M $Na_2Pd(NO_2)_4$ using a current density of 100μA/cm^2 for two hours. Then, the electrolyte was drained off, the compartment washed with distilled water and filled with the anodic solution. The anodic solution (0.2 M NaOH) prior introducing it in the compartment, was prelectrolyzed for at least 24 hours in a separate electrolytic cell. In the anodic compartment the solution was kept at –0.3 V vs Hg/HgO reference electrode until the background current is reduced to less than 3μA/cm^2. Then, the cathodic compartment was filled with the supporting electrolyte and the experiment was carried out. Pre-purified nitrogen was bubbled through both compartments in order to keep them free from oxygen contamination.

Results and Discussion

Tafel and linear sweep voltammetry were used to determine the diagnostic criteria for the identification of the mechanism of hydrogen discharge in the presence and absence of underpotentially deposited Zn, Bi and Pb.

Cyclic Voltammetry Linear sweep voltammetric curves obtained by using an electrolyte containing 1M Na_2SO_4, 0.4 M NaCl, 1M H_3BO_3, pH=4 for different concentrations of zinc ions are given in Figure (1). When starting the cathodic sweep from –0.6 V vs (SCE), two well defined peaks are observed in Figure (1)

when zinc ions are present in the supporting electrolyte. The first peak occurs at –0.950 V vs SCE and is more noble than the Nernst potential of a zinc electrode. The equilibrium potential values of zinc electrode, [E=–1.004 +0.029 lg [Zn^{+2}] are: –1.102 V (SCE); –1.072 V (SCE), –1.042 and –1.034 V (SCE) for investigated zinc ion concentrations of: $5x10^{-4}$ M, $5x10^{-3}$M, $5x10^{-2}$M and 0.1M, respectively. A second peak develops at –1.2 V vs SCE and corresponds to zinc deposition from the bulk of the electrolyte. On the anodic side two stripping peaks at –0.9 V and –0.8 V vs (SCE) occur and correspond to the zinc dissolution and desorption peak. Thus, the shape of the cathodic and anodic curves in Figure (1) indicates that in the presence of zinc ions in the electrolyte at –0.950 V (SCE) and at –0.8 V vs (SCE) an adsorption-desorption process occurs on an AISI 4340 steel membrane with peak currents corresponding to the underpotential deposition and desorption of zinc. According to Figure (1), the zinc deposition peak at –1.2 V (SCE) increases as the zinc content in the electrolyte is increased. This phenomena is not observed for the process occurring at –0.950 V (SCE), indicating that the zinc adsorption on AISI 4340 steel has reached an equilibrium value and does not depend on the amount of the dissolved zinc ions in the electrolyte. Zinc deposition on AISI 4340 steel was also studied at different sweep rates. If the electrodeposition of zinc ions is a transport controlled process, then more zinc will be deposited and subsequently stripped away at low sweep rates. This phenomena is observed in Figure (2) for zinc deposition peak at –1.2 V (SCE). As the sweep rate increases one does not observe any significant change of the zinc adsorption peak area at –0.95 (SCE) indicating that the process

mainly is controlled upon the surface activity and the crystallographic structure of the substrate and that the surface saturation has been completed.

Linear sweep voltammetry was also used to study the nature of lead deposition in AISI 4340 steel from electrolytes containing: 0.5 M $HClO_4$ and 0.25 M $NaClO_4$ at pH=0.3. Again, it has been presumed that a partial monolayer of underpotentially deposited lead on the surface of the substrate will inhibit the hydrogen evolution rate. The potentiodynamic curves obtained for the hydrogen evolution rate in the supporting electrolyte and under identical conditions but in the presence of lead ions are given in Figure (3). When starting the cathodic sweep from –0.3 V (SCE) two well defined peaks are observed. The first peak occurs at – 0.385 V vs SCE and is more noble than the Nernst potential of lead electrode, [E= $-0.368 + 0.029 \lg(2\times10^{-3})$= –0.448 V (SCE). The second peak develops at –0.495 V (SCE) and corresponds to lead deposition from the bulk of the electrolyte. The underpotential shift obtained from the experimental data is ΔE=0.110 V. On the anodic side one stripping peak at –0.4 V (SCE) is observed and corresponds to dissolution of the bulk deposited lead. The shape of the cathodic peaks in Figure (3) indicates that in the presence of lead ions in the electrolyte at –0.385 V an adsorption process occur on the AISI 4340 steel with a peak current corresponding to the underpotential deposition of lead. The amount of charge of the deposited monolayer is determined by the area of the adsorption current maximum and is Q=85 $\mu C/cm^2$. Assuming that the maximum coverage requires a charge of Q_{max}=500 $\mu C/cm^2$ (12), the degree of coverage of lead is θ_{lead}=0.17. Potentiodynamic curves obtained on AISI 4340 steel at different reverse

potentials and in the presence of $2x10^{-3}$ M Pb^{+2} ions are shown in Figure (4). As was expected, increasing the reverse potential more lead is deposited on the substrate resulting in higher maximum of the dissolution peak.

Polarization Measurements-Potentiodynamic Studies The polarization studies were carried out using AISI 4340 steel electrodes with an area of 0.5 cm^2 on which Zn, Bi and Pb were previously deposited. The electrodes were held at fixed cathodic current for a different period of time to ensure the additive deposition on the surface. In order to obtain various coverages a wide range of cathodic currents were applied by trial and error. In the beginning of each experiment the range of current densities at which the additive deposition from the bulk of the electrolyte occurs was determined. Then, several currents below the highest current at which underpotential occurs were used to obtain different surface coverages. The amount of charge required for monolayer deposition was determined by the area of the adsorption-desorption peaks observed in the potentiodynamic studies.

The cathodic polarization curves obtained for hydrogen evolution reaction on bare AISI 4340 steel from electrolyte containing: 1M Na_2SO_4 + 0.4 M NaCl and 1M H_3BO_3, pH=4 and on AISI 4340 steel predeposited with Zn from the same supporting electrolyte in which 0.1 M Zn (II) ions were added are shown in Figure (5). The predeposition was carried out at different current densities for a period of six minutes.

In the absence of zinc, a linear region with a Tafel slope of 127 mV, α_c=0.48 was obtained indicating activation control of h.e.r. in the potential region between –0.590 and –0.760 V vs SCE. The presence of Zn^{+2} ions in the electrolyte inhibited

the h.e.r. and as shown in Figure (5), the Tafel slope is 0.132 V with α_c= 0.44. The results obtained from the polarization studies are summarized in Figure (6), where the dependence of hydrogen evolution current density, measured at –0.7 V (SCE) is presented as a function of the applied predeposition currents. For predeposition current of 600 $\mu A/cm^2$, the hydrogen evolution current is reduced from a value of 572 $\mu A/cm^2$ to 307 $\mu A/cm^2$ (up to two times) compared with the measured current density obtained on bare AISI 4340 steel.

Tafel slopes obtained on AISI 4340 steel with bulk deposited zinc at different predeposition current densities are given in Figure (7). When zinc is deposited from the bulk of the solution an increase of the corrosion potential which results from Zn/electrolyte interface [E_{corr}= –1.050 V (SCE)] is observed in Figure (7). The Tafel slope also increases and has a value of 150 mV with α_c=0.4 and i_o=3.4x10^{-3} $\mu A/cm^2$. The hydrogen current close to the corrosion potential [E=–1.080 mV (SCE)] is between 350 and 400 $\mu A/cm^2$.

As was expected, the underpotential adsorption of zinc onto AISI 4340 steel substrates inhibits the hydrogen evolution reaction due to the kinetic limitations of the hydrogen discharge reaction on the monolayer deposited under underpotential conditions.

Hydrogen evolution reaction was also investigated potentiodynamically on AISI 4340 steel rotating disc electrodes treated with Bi from electrolyte containing: 5x10^{-4} M bismuth oxide, 0.5 M $HClO_4$ and 0.25 M $NaClO_4$. Figure (8) shows the shape of Tafel slope obtained for different currents used in the deposition process and

subsequently for different degrees of surface coverage by bismuth. In absence of bismuth a linear region with a Tafel slope of 0.123 V with α_c=0.48 was obtained, indicating activation control of h.e.r. in the potential region between –0.589 V (SCE) and 0.400 V (SCE). The presence of Bi in the electrolyte, sharply decreases the hydrogen evolution rate with Tafel slope of 0.140 V, α_c=0.4 and a slope of 0.157 V, α_c=0.4 for predeposition currents of 40 μA/cm^2 and 2000 μA/cm^2. The predeposition was carried out for a constant period of time (6 minutes). The hydrogen evolution currents computed at –0.560 V and at –0.6 V (SCE) are given in Figure (9). According to this Figure, with bismuth layers previously deposited on AISI 4340 steel, the hydrogen evolution at –0.56 V vs SCE is reduced drastically up to 20 times compared with hydrogen currents obtained on bare steel.

Figure (10) shows polarizations curves obtained potentiodinamically (scan rate, v=1 mV/s) on AISI 4340 rotating disc electrodes in the electrolyte containing: 0.5 M HCO_4 and 0.25 M $NaClO_4$ in the presence and absence of different concentrations of lead. The presence of lead ions in the electrolyte inhibited the h.e.r. with a Tafel slope of 0.129 V and α_c=0.45. As shown in Figure (11), the hydrogen evolution current on previously underpotentially deposited lead [at –0.58 V (SCE)] on AISI 4340 rotating disc electrodes decreases from 1.9 mA/cm^2 (value measured on bare steel in supporting electrolyte) to 1.064 mA/cm^2.

The polarization experiments carried out in the presence of lead in the electrolyte indicate that the underpotential deposited lead inhibits the adsorption step in the hydrogen evolution reaction which results in an increase of the h.e.r. overpotential.

Potentiostatic Measurements Two basic mechanism have been accepted for hydrogen evolution. These are recombination mechanism expressed as:

$$H^+ + e^- + M \overset{k_1}{\mapsto} MH_{ads} \tag{1}$$

$$MH_{ads} + MH_{ads} \mapsto 2M + H_2 \tag{2}$$

and the electrochemical desorption mechanism:

$$M + H^+ + e^- \mapsto MH_{ads} \tag{3}$$

$$MH_{ads} + H^+ + e \mapsto H_2 + M \tag{4}$$

According to Bockris et al. (14) and McBreen et al. (15), the hydrogen evolution reaction on an iron substrate in acidic electrolytes is determined by the coupled discharge - recombination mechanism. Assuming the Langmuir adsorption isotherm, Subramanyan et al. (1) have shown theoretically that the discharge-recombination mechanism is released at low degree of surface coverage by atomic hydrogen (θ<0.1). Thus one can expect that a partial monolayer of underpotentially deposited zinc, bismuth and lead on the most active adsorption centres on the substrate will inhibit the hydrogen reaction.

Assuming, the Temkin adsorption isotherm (16), the discharge-recombination mechanism is released under conditions where the hydrogen coverage is not low and

the interaction between the adsorbed atoms becomes appreciable. Also, different sites on the substrate surface may have different free energies for hydrogen absorption.

In order to determine the diagnostic criteria for the identification of the mechanism of the discharge of hydrogen ions on AISI 4340 steel, separate experiments were carried out with the supporting electrolyte in which the hydrogen cathodic current density was measured as a function of the applied overpotential. In these experiments, the alloy membrane on the cathodic side of the cell was polarized potentiostatically. The current-potential relationship is presented in Figure (12), where two different slopes are observed. At low overpotentials the slope is $\frac{\partial \eta}{\partial \log I_c}$ is 0.118 V which corresponds to $\frac{2RT}{F}$ diagnostic criteria indicating that the mechanism of the hydrogen evolution reaction is coupled discharge-recombination with Langmuir isotherm for hydrogen coverage (15). Thus, one can conclude that in the investigated supporting electrolyte, the hydrogen ion discharge proceeds under simultaneous control of the discharge and recombination stages. At higher overpotentials, the current vs potential plot gives a slope of 0.177, which corresponds to $\frac{3RT}{F}$ diagnostic criteria, which indicates that the h.e.r has the same mechanism but with Temkin isotherm of hydrogen coverage (15). The transfer coefficients calculated by using these two sets of data are 0.52 and 0.50 respectively. A value of 0.51 for the transfer coefficient is used in all calculations. Figure (13) shows the dependence of the steady state hydrogen permeation current j_∞ upon the overpotential. This plot also provides a diagnostic criteria for the identification of the mechanism of the discharge of hydrogen ions on an iron membrane. At lower overpotentials the slope $\frac{\partial \eta}{\partial \ln j_\infty} = \frac{4RT}{F}$ which

is consistent with the previously discussed $\frac{d\eta}{d\ln I_c}$ criteria which indicates a coupled discharge-recombination mechanism. However, at higher overpotentials the slope of the steady state hydrogen permeation current vs overpotential plot is different than the expected value of 3RT/2F, a diagnostic criteria for a coupled discharge - recombination mechanism with Temkin isotherm (15).

Hydrogen Permeation Studies. In the preliminary permeation experiments, the hydrogen permeation transients were obtained in supporting electrolyte containing: 0.5 M $HClO_4$ and 0.25 M $NaClO_4$ in the absence of the additives. The atomic hydrogen permeation current densities vs time for different overpotentials are plotted in Figure (14). As seen in Figure (14), the steady state hydrogen permeation current increases with the increase of the applied cathodic potential until the overpotential reaches a value of –0.6 V (SCE). Above this potential, the steady state hydrogen permeation current is independent upon the applied potential. Similar complex behavior of the hydrogen permeation transients has been also observed (17–18). The diffusion of hydrogen through the AISI 4340 steel membrane was calculated [by using the data at E_c=– 0.690 V (SCE)] to be 3.2 x 10^{-7} cm^2/s. When carrying out experiments with a bipolar membrane, the steady sate rate of hydrogen penetration in a diffusion mode can be presented by the following equations obtained for two typical boundary conditions: (1) in the case when the hydrogen concentration at the entry side of the membrane is constant (19);

$$\frac{j_t - j_o}{j_\infty - j_o} = 1 + 2\sum_{n=1}^{\infty}(-1)^n exp(-n^2\pi^2\tau) \qquad (5)$$

(2) in the case when the flux of the hydrogen entering the membrane is constant (19);

$$\frac{j_t - j_o}{j_\infty - j_o} = 1 - \frac{4}{\pi}\sum_{n=0}^{\infty}\frac{(-1)^n}{(2n+1)}exp\left\{-\frac{(2n+1)^2\pi^2\tau}{4}\right\} \qquad (6)$$

where j_t = transition hydrogen permeation current density; j_o= initial hydrogen permeation current density (may or may not be zero); j_∞= steady state hydrogen permeation current density. In Figure (15), the hydrogen permeation current vs the dimensionless time τ and the theoretical solutions for the two typical boundary conditions given above are presented for comparison with the experimental results given in Figure (14). According to Figure (15), at high cathodic overvoltages, the experimental permeation curves are close to the theoretical curve obtained when the boundary condition is a constant hydrogen concentration at the entry side of the membrane. At lower applied cathodic overpotentials as seen in Figure (15), the experimental permeation transients are approaching the theoretical curve obtained by using boundary conditions in which the flux of the hydrogen entering the membrane is constant.

Using the mechanistic model developed by Iyer et al. (20-21), the hydrogen surface coverage and the surface concentration, the hydrogen absorption, discharge and recombination rate constants as well as the h.e.r coverage-dependent transfer coefficient, α, and the exchange current density i_o were computed from a knowledge of the steady state hydrogen permeation current, cathodic charging current, hydrogen diffusivity and hydrogen overvoltage.

Assuming that the recombination step of hydrogen evolution is not rate-determining so that the hydrogen atom oxidation can be neglected (η>RT/F) and if the Langmuir

isotherm is used to describe the hydrogen coverage of the substrate, the cathodic charging current values may be determined by the following equation:

$$i_c = i_o'(1-\theta_H)e^{-a\alpha\eta} \tag{7}$$

where θ_H is the hydrogen surface coverage, a =F/RT, α is the transfer coefficient, η= hydrogen overvoltage and

$$i_o' = \frac{i_o}{1-\theta_e} \tag{8}$$

where i_o= the exchange current density and θ_e is the hydrogen surface coverage at equilibrium.

Assuming that the hydrogen evolution mechanism is a coupled discharge - recombination process and Langmuir conditions are assumed for the hydrogen coverage, the hydrogen recombination current is:

$$i_r = Fk_3\theta_H^2 \tag{9}$$

where k_3 is the recombination rate constant.

Assuming that the hydrogen permeation current density is described by a simple diffusion model through the membrane without trapping once the steady state is reached, the analytical solution for the hydrogen steady state permeation flux is as follows:

$$j_\infty = \frac{FD}{L}C_s = \frac{C_s}{b} \tag{10}$$

where b=L/FD, L= the membrane thickness, D=hydrogen diffusion coefficient and C_s is the surface hydrogen concentration.

In the case when the intermediate hydrogen adsorption-absorption reaction is in local equilibrium and Langmuir isotherm applies, the hydrogen surface concentration C_s may be computed from:

$$C_s = k'' \theta_H \tag{11}$$

where

$$k'' = \frac{k_{abs}}{k_{ads} + \frac{D}{L}} \tag{12}$$

where k_{abs} is the absorption rate constant and k_{ads} is the adsorption rate constant.

By combining the Equations (9), (10) and (11) the following equation may be computed for the hydrogen steady state permeation flux:

$$j_\infty = \frac{k''}{b\sqrt{F k_3}} \sqrt{i_r} \tag{13}$$

Combining the Equations (7), (10), and (11) one obtains the dependence between the hydrogen charging current and the hydrogen steady state permeation flux through the membrane:

$$i_c e^{a\alpha\eta} = -\frac{b i_o'}{k''} j_\infty + i_o' \tag{14}$$

However, in many cases, the hydrogen discharge and recombination reactions are activated in which case Frumkin-Temkin corrections (16) have to be applied for θ_s in the equations for the hydrogen charging current and hydrogen recombination current.

With Frumkin-Temkin corrections applied, in the Equations of i_c and i_r, one obtains:

$$i_c = i_o'(1-\theta_s)e^{-\alpha f\theta_s}e^{-a\alpha\eta} \tag{15}$$

$$i_r = Fk_3\theta_s^2 e^{2\alpha f\theta_s} \tag{16}$$

Applying the same corrections to Equations (13) and (14):

$$ln\left(\frac{\sqrt{i_r}}{j_\infty}\right) = \frac{\alpha f b}{k''}j_\infty + ln\left(\frac{b\sqrt{Fk_3}}{k''}\right) \tag{17}$$

and

$$ln\left(\frac{i_c e^{\frac{afbj_\infty}{k''}}}{1-\frac{bj_\infty}{k''}}\right) = -\alpha a\eta + lni_o' \tag{18}$$

where f= γ/RT and γ= the gradient of the apparent standard free energy of adsorption with coverage. The value of f=4 to 5 for hydrogen coverages (21).

Equations (13) and (14) or Equations (17) and (18) may be used to compute various reactions parameters such as k_3, k'' and i_o'.

Figure (16) shows the dependence of the steady state permeation current upon the square root of the cathodic charging current. A linear relationship is obtained at lower overpotentials which is consistent with Equation (13). In Figure (17), $i_c e^{a\alpha\eta}$ is plotted vs j_∞. Using the slopes and intercepts in Figure (16) and Figure (17) and Equations (12) and (13), the values of the exchange current density, k'' and k_3 were computed to be 7.2×10^{-6} A/cm^2; 4.1×10^{-4} mol/cm^3 and 1.1×10^{-6}mol/cm^{2}s, respectively. Substituting the calculated k_3 value of 1.1×10^{-6} and experimentally

measured $i_r = i_c - j_\infty$ in Equation (9), the hydrogen surface coverage was calculated and is presented in Figure (18) as a function of the hydrogen overpotential.

Several points at high overpotentials do not fit both, the Equation (13) and Equation (17) due to the fact that at these overpotentials the j_∞ is independent of the hydrogen recombination current.

As already discussed, at high overpotentials, the permeation flux reaches the steady state value probably due to the fact that the hydrogen coverage θ_H reaches its saturated value and no longer increases with the increase of the applied cathodic potential. In such a case as seen in Equations (10) and (11) the permeation current is independent of the cathodic current. Thus, the last three points at high hydrogen overpotentials in Figure (18) may not represent the actual relationship between the hydrogen surface coverage and the overpotential.

As shown in our corrosion studies monolayer coverage of Pb, Bi and Zn adatoms cause a suppression of hydrogen adsorption by changing chemically the substrate surface. As a consequence, the hydrogen absorption process is altered without changing the mechanical or physical properties of the substrate.

In order to investigate if any inhibition of the hydrogen permeation current occurs in the presence of the additives, the hydrogen permeation experiments were carried out in the presence of Zn^{+2}, Bi^{+3} and Pb^{+2} using in the cathodic compartment the same supporting electrolytes as those used in the corrosion studies.

As shown in our potentiodynamic and corrosion studies in supporting electrolyte

containing 1M Na_2SO_4, 0.4 M NaCl, 1M H_3BO_3 and 0.1 M $ZnCl_2$, the underpotential deposition of Zn occurs at –1.0 V (SCE). Thus, in order to study the influence of Zn^{+2} ions on hydrogen permeation, the permeation experiments were carried out at a discharge potential of –1.0 V in the presence and absence of 0.1 M Zn^{+2} ions. The resulting hydrogen permeation transients are plotted in Figure (19). According to this Fugure, the steady state hydrogen flux is reduced from 19.7 $\mu A/cm^2$ to 9.5 $\mu A/cm^2$, (a decrease of about 52%) and is partially due to the observed decrease of the steady state discharge current density (decreases from 26.6 mA/cm^2 to 21.3 mA/cm^2).

Equation (13) written for a case when the zinc ions are present and absent in the electrolyte becomes:

$$j_{\infty,1} = \frac{k_1''}{b\sqrt{F k_{3,1}}}\sqrt{i_{r,1}} \tag{19}$$

$$j_{\infty,2} = \frac{k_2''}{b\sqrt{F k_{3,2}}}\sqrt{i_{r,2}} \tag{20}$$

where subscript 1 and 2 and denotes absence and presence of the additives. Dividing the Equations (19) and (20), one obtains:

$$\frac{j_{\infty,2}}{j_{\infty,1}} = \sqrt{\frac{i_{r,2}}{i_{r,1}}}\sqrt{\frac{k_{3,1}}{k_{3,2}}}\frac{k_2''}{k_1''} \tag{21}$$

According to Equation (21), the hydrogen permeation flux may be reduced due to: (1) the changes of the surface properties, i.e., the increase of the hydrogen recombination rate constant (k_3) or (2) by decreasing the absorption-adsorption constant (k''). Our objective was by using the additives to modify the surface in order to achieve these favorable changes and to reduce the hydrogen permeation flux.

Substituting the value obtained for steady state permeation flux and the value of i_r, Equation (21) becomes:

$$0.54 = \frac{k_2''}{k_1''}\sqrt{\frac{k_{3,1}}{k_{3,2}}}. \qquad (22)$$

The hydrogen permeation through AISI 4340 steel membrane was also studied in the presence of Bi^{+3} and Pb^{+2} in the supporting electrolyte containing 0.5 M $HClO_4$ and 0.25M $NaClO_4$. In order to avoid the bulk deposition of Bi^{+3} and Pb^{+2} on the steel substrate, an underpotential deposition of the additives was ensured by keeping the applied potential (according to our potentiodynamic and corrosion studies) in the range between –0.6 V vs SCE and –0.710 V (SCE). The resulting hydrogen permeation transients obtained for Bi^{3+} and Pb^{+2} are shown in Figure (20) and Figure (21), respectively. In the presence of bismuth ions in the supporting electrolyte, the steady state hydrogen flux at –0. 6 V (SCE) is reduced by 65%, while at –0.710 V (SCE) by 56%. In the presence of lead ions in the electrolyte, the steady state hydrogen flux at –0. 6 V (SCE) is reduced by 71%, while at applied potential of -0.710 V (SCE), the flux is reduced by 67%.

The hydrogen permeation studies carried out from conventional bismuth, lead or zinc plating solution show that the underpotential deposition of submonolayers of lead, bismuth or zinc inhibit the hydrogen evolution rate and the degree of hydrogenation ingress into AISI 4340 steel. Further work in order to determine the dependence of hydrogen permeation current upon overpotentials in the presence of the additives is in progress. These studies will clarify the contribution of the surface properties, namely

the hydrogen recombination constant and the absorption - adsorption constant [when zinc, bismuth or lead are underpotentially deposited] on the hydrogen permeation and will result in development of a method for the elimination of the hydrogenation hazards.

Conclusion

The polarization experiments show, that deposited zinc, bismuth and lead effectively inhibit the discharge of hydrogen up to 20 times compared with the value obtained on bare steel. The observed inhibition effect is due to an underpotential deposition of these metal ions which built a complete two dimensional adsorbate layer at the following potentials:

$$E_{Me/Me^{z+}} \leq E_{u.p.} \leq E_{Me/Me^{z+}} + 80mV \left[Me^{z+} = Zn^{+2}, Bi^{+3}, Pb^{+2}\right] \qquad (23)$$

The hydrogen cathodic current density was measured potentiostatically as a function of the applied overpotential to determine the diagnostic criteria for the identification of the mechanism of the discharge of hydrogen ions on AISI 4340 steel. At low overpotentials, the slope is 0.118 V has been obtained which corresponds to a value of 2RT/F indicating that the mechanism of the hydrogen evolution reaction is coupled discharge-recombination with Langmuir isotherm for hydrogen coverage. At higher overpotential, the current vs potential plot gives a slope of 0.177, which corresponds to a value 3RT/F which indicates that h.e.r. has the same mechanism but

with Temkin isotherm of hydrogen coverage. The transfer coefficients calculated by using these two sets of data are 0.52 and 0.50 respectively. The dependence of the steady state hydrogen permeation current upon the overpotential gives a slope which correspond to 4RT/F which is consistent with the slope obtained from $d\eta/d\ln I_c$ criteria indicating at low overpotentials a coupled discharge-recombination mechanism for hydrogen discharge.

The hydrogen surface coverage and the surface concentration, the hydrogen absorption, discharge and recombination rate constants as well as the h.e.r. coverage-dependent transfer coefficient, α, and the exchange current density i_o were computed from a knowledge of the steady state hydrogen permeation current, cathodic charging current, hydrogen diffusibility and hydrogen overvoltage. The best inhibition of the hydrogen permeation rate through the membrane was obtained with an underpotential deposited lead onto the AISI 4340 steel which reduces the steady state hydrogen flux by 71 %.

Acknowledgment

Technical assistance and financial support by A. John Sedriks, the Office of Naval Research, under Contract No N00014–92–J-1434 are gratefully acknowledged.

List of Symbols

$a = F/RT$, $(V)^{-1}$

$b = L/(FD_H)$, $(Acm)^{-1}$)

C_s= surface hydrogen concentration, (mol cm^{-3})

D = hydrogen diffusion coefficient, (cm^2 s^{-1}

F = Faraday constant, 96,500 C $(g\text{-}eq)^{-1}$

L = membrane thickness, (m)

i_o = exchange current density, (A cm^{-2}).

$i_o' = \frac{i_o}{1-\theta_e}$, (A cm^2)

j_t = transition hydrogen permeation current density, (A cm^{-2})

j_o = initial hydrogen permeation current density, (A cm^{-2})

j_{oo} = steady state hydrogen permeation current density, (A cm^{-2})

k_{abs} = absorption rate constant, [mol $(cm^2 s)^{-1}$]

k_{ads} = adsorption rate constant, (cm s^{-1})

k_3 = recombination rate constant, [mol $(cm^2 s)^{-1}$]

k" = thickness dependent absorption-adsorption constant, (mol cm^{-3}).

Greek Symbols

α = transfer coefficient, dimensionless

θ_e = equilibrium hydrogen surface coverage, dimensionless

θ_H = hydrogen surface coverage, dimensionless

γ = gradient of the apparent standard free energy of adsorption with hydrogen coverage, [J (g-mol)$^{-1}$]

η = overvoltage, (V).

$\tau = t\ D/L^2$ = dimensionless time

Figure Captions

Figure (1) Potentiodynamic curves obtained on AISI 4340 rotating disc electrode (RDE) by using an electrolyte containing 1M Na_2SO_4, 0.4M NaCl, 1M H_3BO_3 at pH=4, for different concentrations of Zn^{+2}. Sweep rate, v= 100mV/s

Figure (2) Potentiodynamic curves obtained on AISI-4340 RDE at different sweep rates from the same electrolyte as in Figure(1) in the presence of Zn^{+2}. $C_{Zn^{+2}}$= $5x10^{-2}$M.

Figure (3) Potentiodynamic curves obtained on AISI 4340 RDE by using electrolyte containing 0.5M $HClO_4$ and 0.25M $NaClO_4$ at pH=3 ion the absence and presence of $2x10^{-3}$M Pb^{+2}. Sweep rate, v=500 mV/s.

Figure (4) Potentiodynamic curves obtained on AISI 4340 RDE by using the same supporting electrolyte as in Figure (3) in the presence of $2x10^{-3}$M Pb^{+2} at different vertex potentials. Sweep rate, v=500mV/s.

Figure (5) Cathodic polarization curves obtained on AISI 4340 RDE by using electrolyte containing 1M Na_2SO_4, 0.4M NaCl, 1M H_3BO_3 at pH=4, and on AISI 4340 RDE, predeposited with zinc from electrolyte containing 0.1m Zn^{+2}. Scan rate, v=1mV/s.

Figure (6) Dependence of hydrogen evolution current on AISI 4340 RDE computed at –0.700V (SCE) as a function of the applied predeposition current.

Figure (7) Cathodic polarization curves recorded on AISI 4340 RDE with bulk deposited zinc obtained by applying different current densities from the same supporting electrolyte as in Figure (5) in the presence of 0.1M Zn^{+2}.

Figure (8) Cathodic polarization curves obtained on AISI 4340 RDE by using electrolyte containing: 0.5M $HClO_4$ and 0.25M $NaClO_4$ in the absence and presence of $5x10^{-4}$M Bi^{+3}. The predeposition was carried out for 5 minutes using different current densities. Scan rate, v=1mV/s.

Figure (9) Dependence of hydrogen evolution current on AISI 4340 RDE computed at –0.560V, (SCE) and at –0.500V, (SCE) as a function of the applied current.

Figure (10) Cathodic polarization curves obtained on AISI 4340 RDE by using electrolyte containing: 0.5M $HClO_4$ and 0.25M $NaClO_4$ in the absence and presence of different concentrations of Pb^{+2}. Scan rate, v=1mV/s.

Figure (11) Dependence of hydrogen evolution current on AISI 4340 RDE,

computed at –0.580V (SCE) as a function of Pb^{+2} concentration in the electrolyte.

Figure (12) Current–overpotential relationship for hydrogen evolution reaction obtained on AISI 4340 RDE in the same supporting electrolyte as in Figure (10).

Figure (13) Hydrogen permeation current-overpotential dependence obtained on AISI 4340 steel membrane in the same supporting electrolyte as in Figure (10).

Figure (14) The atomic hydrogen permeation transients through AISI 4340 membrane as a function of time for different applied overpotentials.

Figure (16) Hydrogen permeation transients as a function of the dimensionless time τ. The theoretical solutions for the two typical boundary conditions are compared with the experimental results given in Figure (14).

Figure (17) Plot of hydrogen permeation current vs. square root of the cathodic current density.

Figure (18) Plot of $i_c e^{a\alpha\eta}$ as a function of hydrogen permeation.

Figure (19) Plot of hydrogen coverage as a function of the overpotential on AISI

4340 membrane.

Figure (20) Hydrogen permeation transients through AISI 4340 steel membrane obtained at E_c= –1.0V (SCE) in the presence and absence of Zn^{+2}.

Figure (21) Hydrogen permeation transients through AISI 4340 steel membrane at E_c= —0.710V (SCE) in the presence and absence of Bi^{+3} and Pb^{+2}.

Figure (22) Hydrogen permeation transients through AISI-4340 steel membrane at E_c= –0.600V (SCE) in the absence and presence of Bi^{+3} and Pb^{+2}

References

1. P. Subramanyan in *"Comprenhensive Treatise of Electrochemistry"*, J. O'M Bockris, Brian E. Conway, Ernest Yeager and Ralph E. White, Eds., **4**, p. 411, Plenum Press, New York, (1981).
2. S. Bagaev and K. Pedan and V. Kudrjavtsev, *Zatshtita Metallov*, **19**, 968 (1983).
3. V. Kudryatsev, K. Pedan, H. Barbashkina and S. Vagramjan, **ibid**, **9**, 161, (1973).
4. J. J. Reilly, *Z. Phys. Chem.* **117**, 655, (1979).
5. D. M. Drazic and L. Z. Vorkapic, *Corrosion Science*, **18**, 907, (1978).
6. A. Despic and M. Pavlovic, *Electrochim. Acta*, **27**, 1539, (1982).
7. K. Juttner, *Werkst. Korros.*, **31**, 358, ((1980).
8. A. M. Abd El Halim, K. Juttner and W. J. Lorenz, *J. Electroanal. Chem.*, **106**, 193, (1980).
9. N. Faruya and S. Motoo, *ibid*, **70**,165, (1976); **78**, 243 (1977); **88**, 151, (1978).
10. G. Lafranconi, F. Mazza, E. Sivieri and S. Torchio, *Corrosion Scieence*, **18**, 617, (1978).
11. S. H. Cadle and S. Bruckenstein, *Anal. Chem.*, **43**, 1858, (1971).
12. V. Kudryavtsev, K. Pedan and S. Bagaev, *J. Electroanal. Chem.*, **248**,421, (1988).
13. M. A. V. Devanathan and L. Strachurski, *Proc. R. Soc. London Ser*, **A, 270**, 90, (1962).
14. J. O'M. Bockris, J. McBreen and L. Nanis, *J. Electrochem. Soc.*, **112**, p. 1027, (1965).

15. J. McBreen and A. M. Genshow, *Proc. Conf. Fund Aspects of Stress Corrosion Cracking, NACE*, Columbus, OH, p. 51 (1969).

16. A. N. Frumkin, *Advances in Electrochemistry and Electrochemical Engineering*, Vol. III, Ed. P. Delahay, Interscience, p. 287, New York, (1963).

17. W. Raczynski, *Archiwum Hutnictwa* 3, 59, (1958).

18. T. Zakroczymski, Z. Szklarska-Smialowks, and M. Smialowski, *Werkst. Korros.*, 26, 617, (1975).

19. N. Boes and H. Zuchner, *J. Less-Common Metals*, 49, 223 (1976).

20. R. N. Iyer, H. W. Pickering and M. Zamanzadeh, *J. Electrochem. Soc.*, 136, 2463, (1989).

21. R. N. Iyer, H. W. Pickering and M. Zamanzadeh, *Scripta Metallurgica*, 22, 911, (1988).

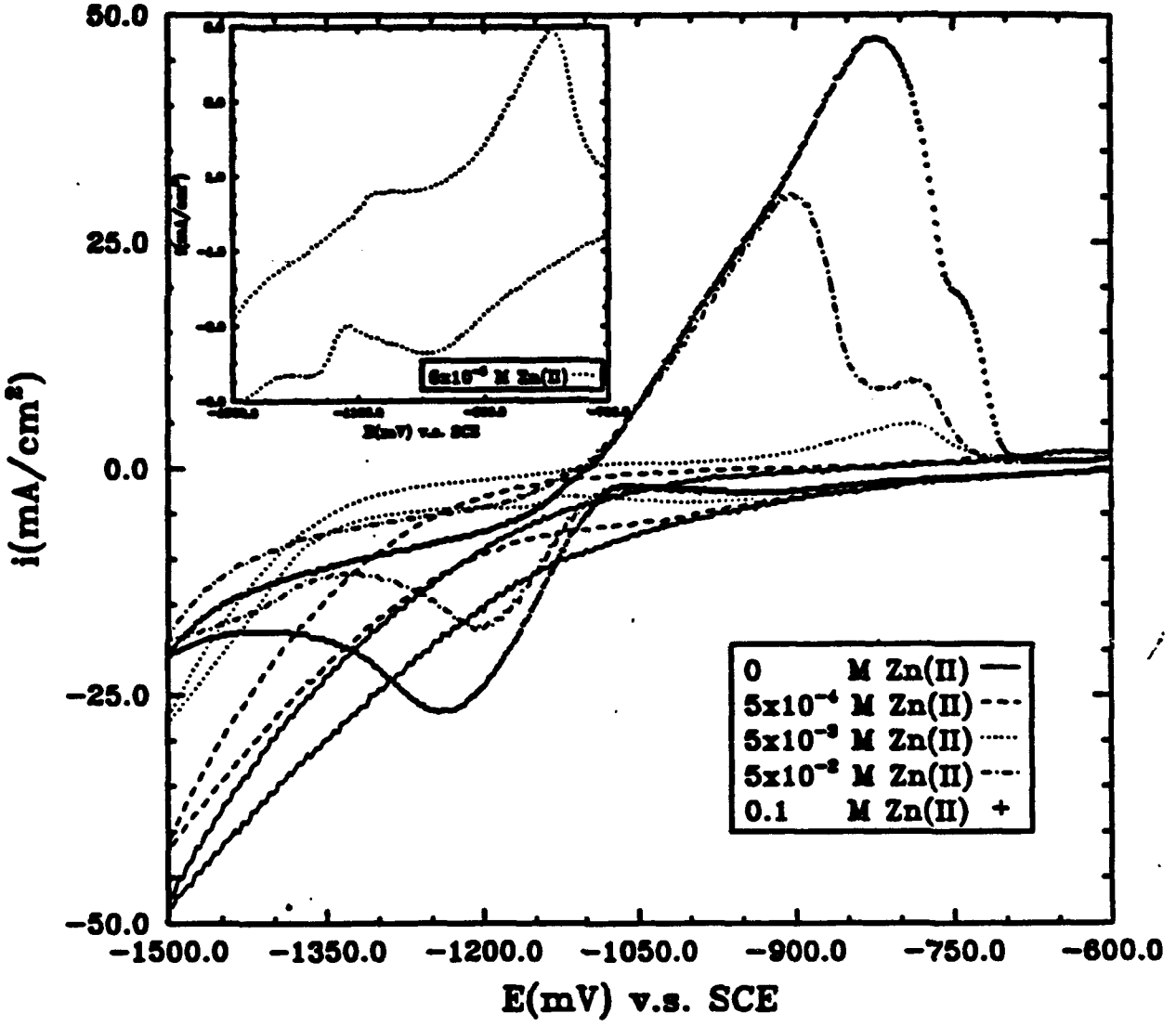
50.0
25.0
0.0
-25.0
-50.0
i(mA/cm²)
-1500.0
-1350.0
-1200.0
-1050.0
-900.0
-750.0
-600.0
E(mV) v.s. SCE
0 M Zn(II)
5x10⁻⁴ M Zn(II)
5x10⁻³ M Zn(II)
5x10⁻² M Zn(II)
0.1 M Zn(II)

Figure 1

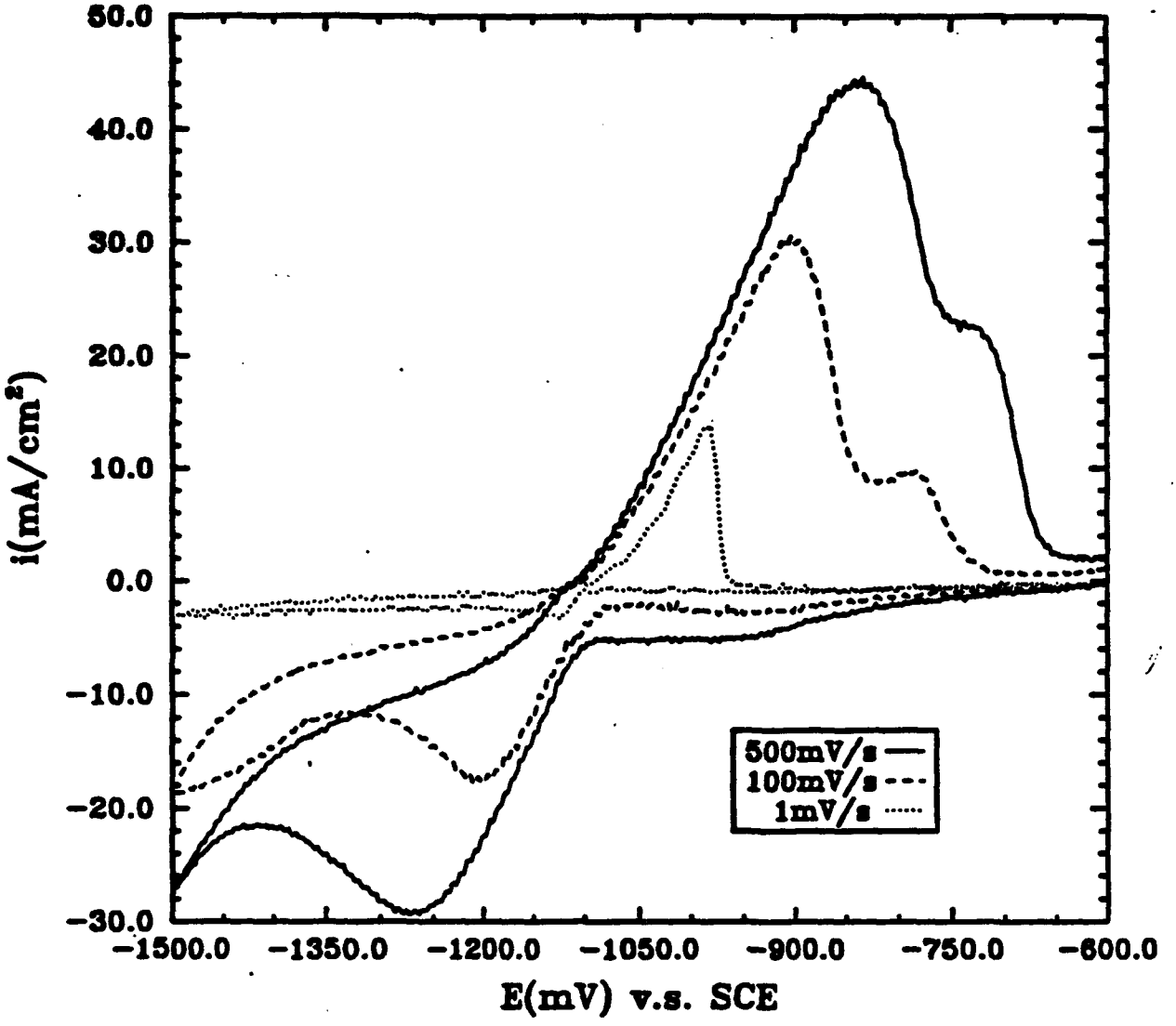
50.0
40.0
30.0
20.0
10.0
0.0
-10.0
-20.0
-30.0
i(mA/cm²)
-1500.0
-1350.0
-1200.0
-1050.0
-900.0
-750.0
-600.0
E(mV) v.s. SCE
500mV/s
100mV/s
1mV/s

Figure 2

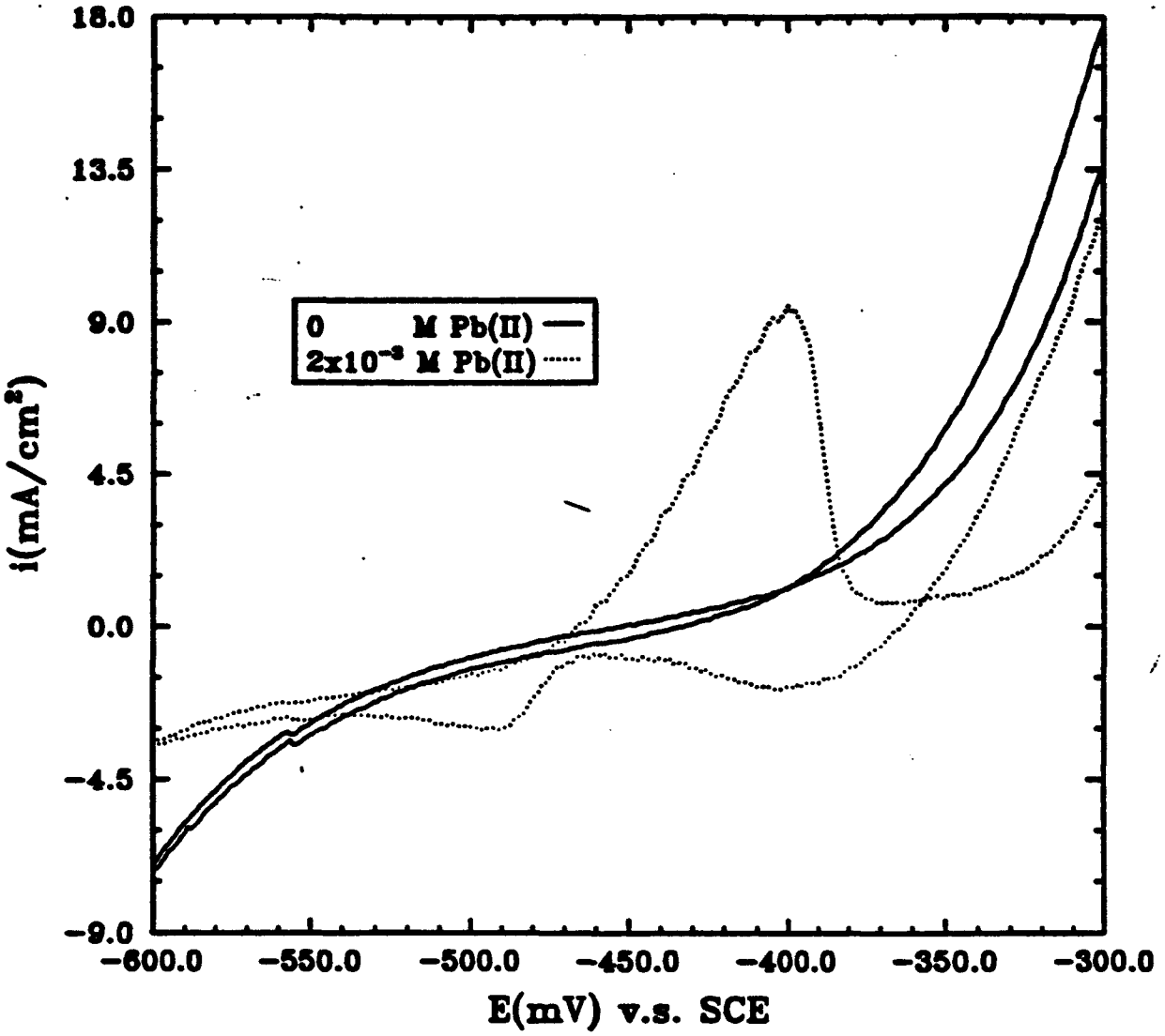
18.0
13.5
9.0
4.5
0.0
-4.5
-9.0
i(mA/cm²)
0 M Pb(II)
2x10⁻³ M Pb(II)
-600.0
-550.0
-500.0
-450.0
-400.0
-350.0
-300.0
E(mV) v.s. SCE

Figure 3

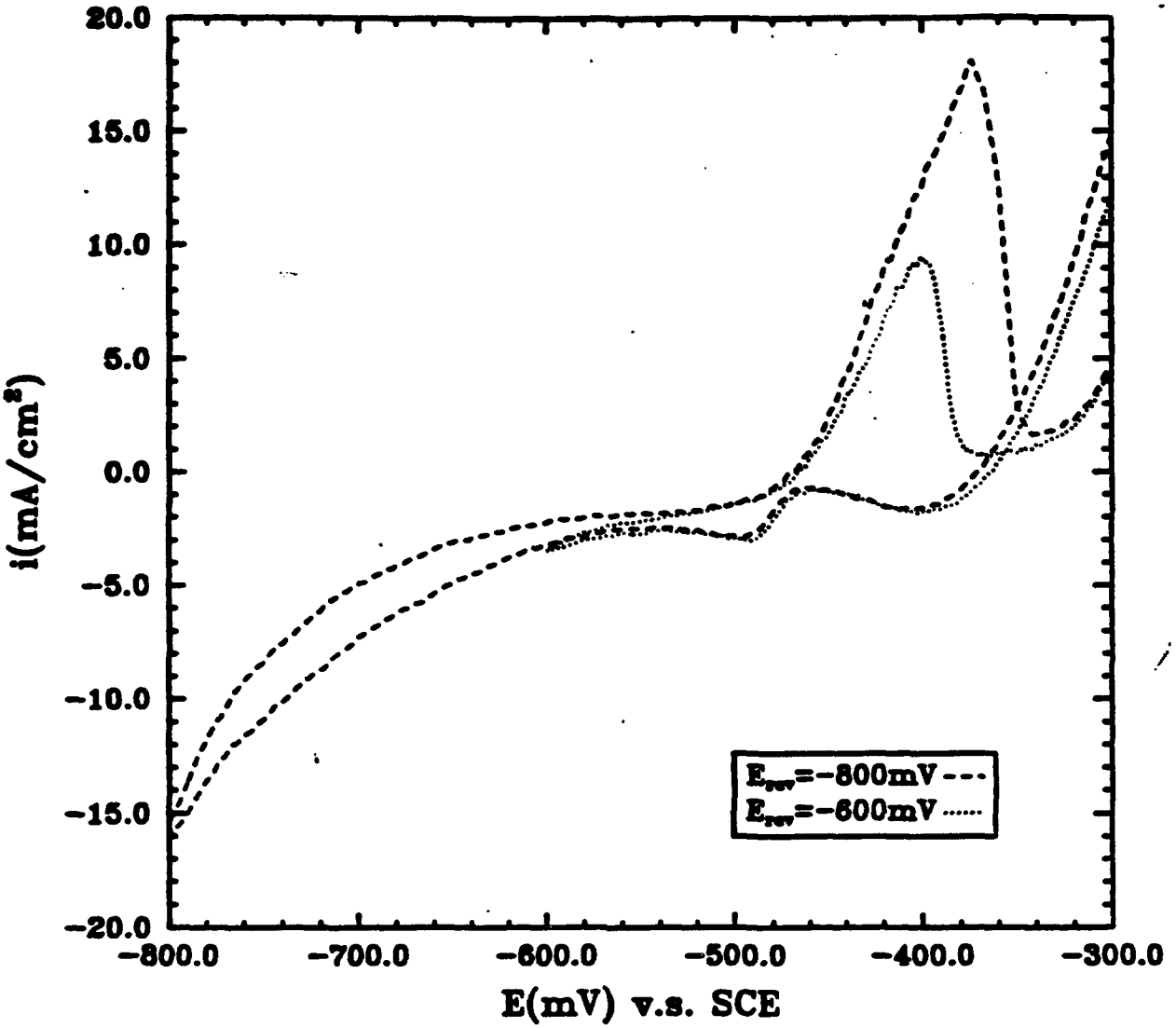
20.0
15.0
10.0
5.0
0.0
-5.0
-10.0
-15.0
-20.0
i(mA/cm²)
-800.0
-700.0
-600.0
-500.0
-400.0
-300.0
E(mV) v.s. SCE
E_rev=-800mV
E_rev=-600mV

Figure 4

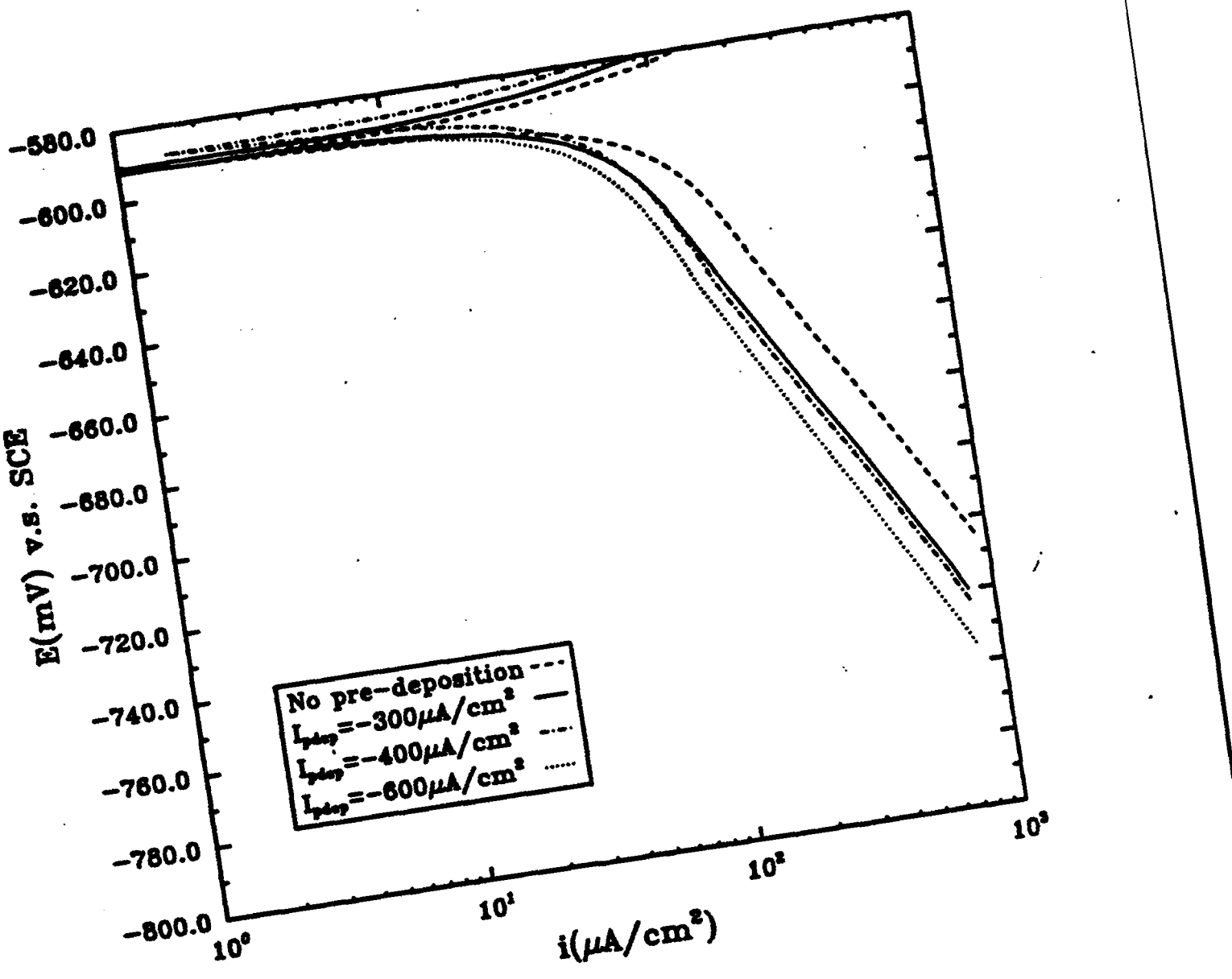
E(mV) v.s. SCE
-580.0
-600.0
-620.0
-640.0
-660.0
-680.0
-700.0
-720.0
-740.0
-760.0
-780.0
-800.0
10⁰
10¹
10²
10³
i(μA/cm²)
No pre-deposition
I_plap=-300μA/cm²
I_plap=-400μA/cm²
I_plap=-600μA/cm²

Figure 5

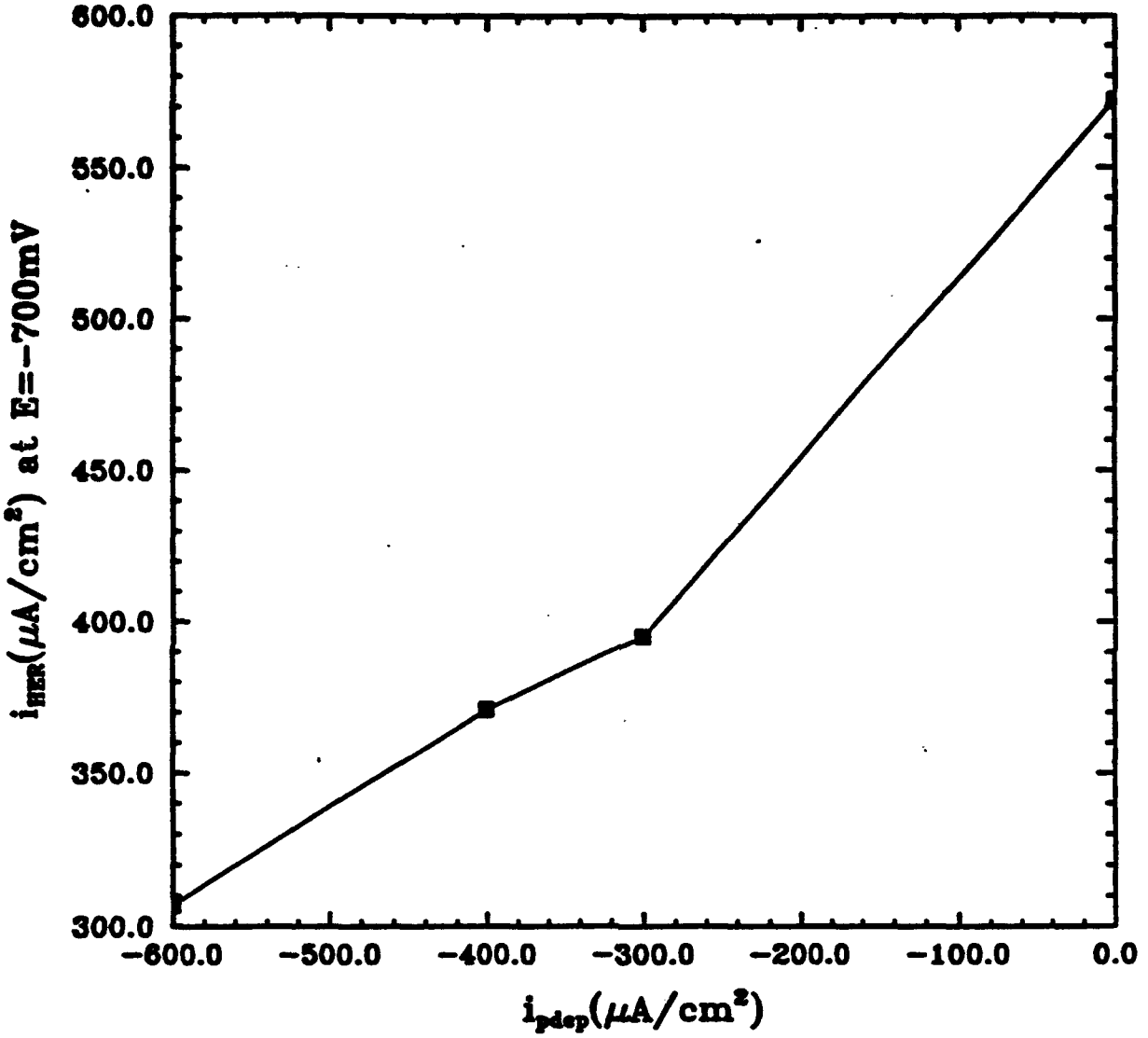
600.0
550.0
500.0
450.0
400.0
350.0
300.0
$i_{MER}(\mu A/cm^2)$ at E=-700mV
-600.0
-500.0
-400.0
-300.0
-200.0
-100.0
0.0
$i_{pdep}(\mu A/cm^2)$

Figure 6

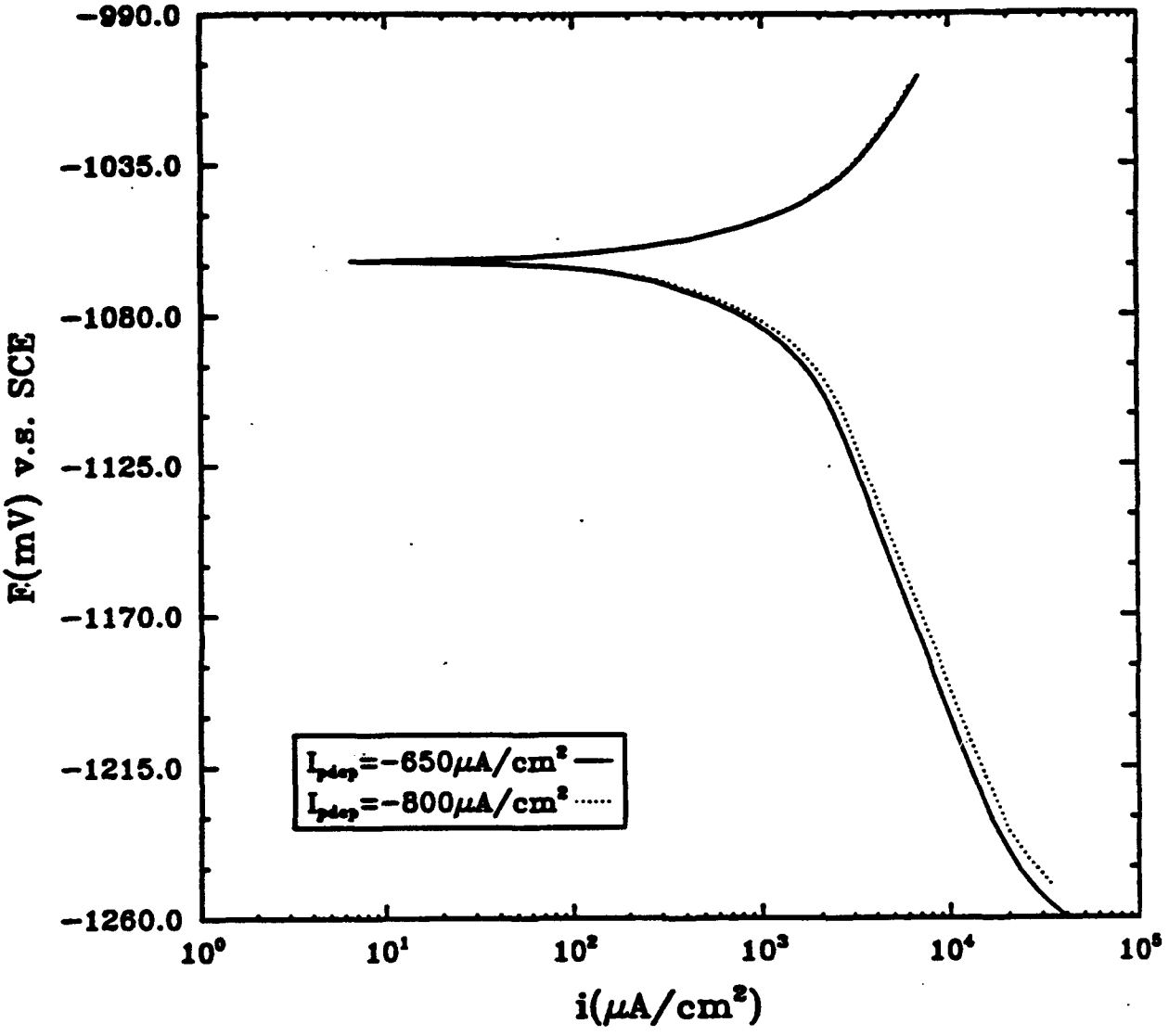
-990.0
-1035.0
-1080.0
-1125.0
-1170.0
-1215.0
-1260.0
E(mV) v.s. SCE
10^0
10^1
10^2
10^3
10^4
10^5
i(μA/cm²)
I_{pdep}=-650μA/cm² —
I_{pdep}=-800μA/cm² .....

Figure 7

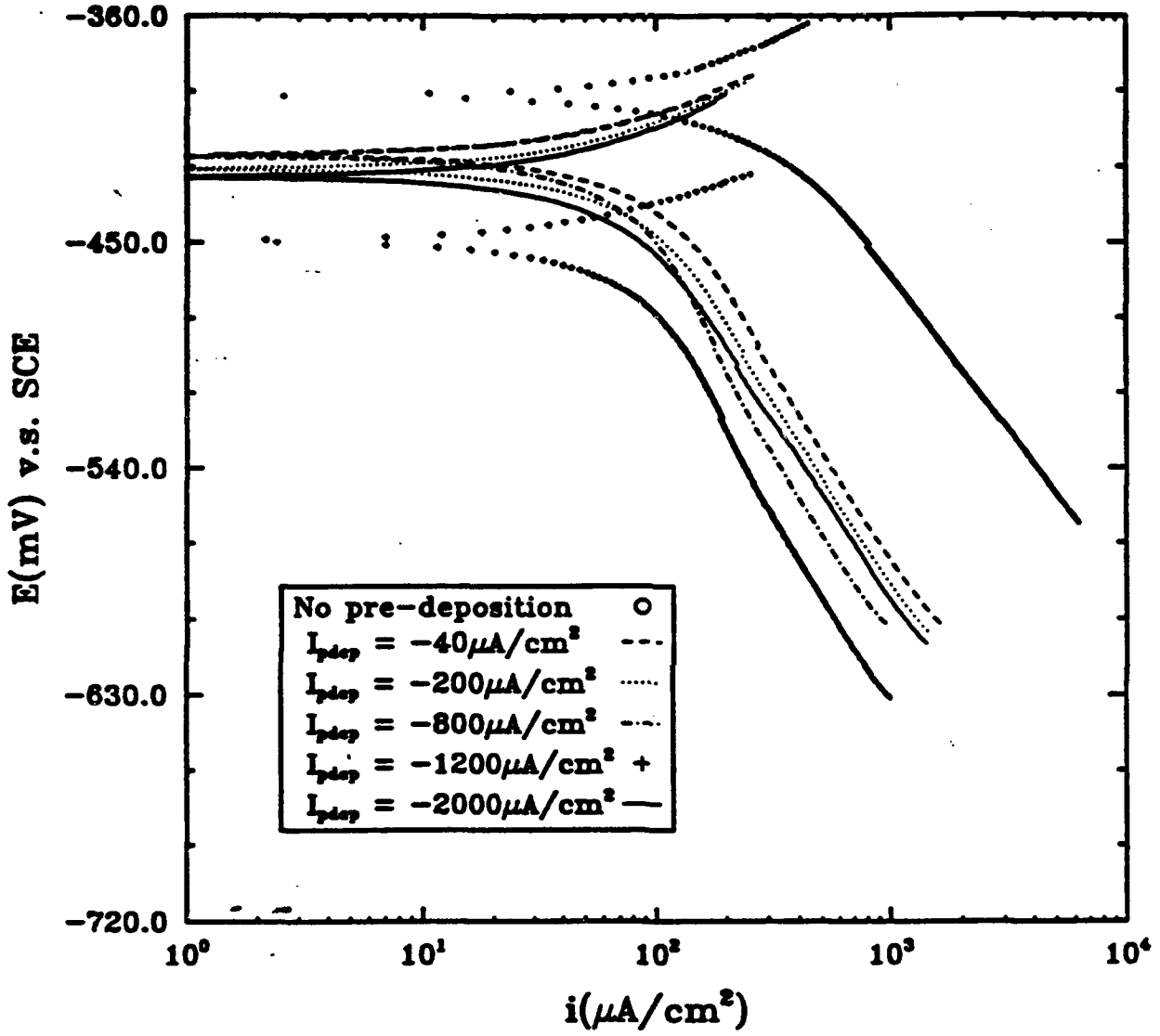
-360.0
-450.0
-540.0
-630.0
-720.0
E(mV) v.s. SCE
10⁰
10¹
10²
10³
10⁴
i(μA/cm²)
No pre-deposition
I_pdep = -40μA/cm²
I_pdep = -200μA/cm²
I_pdep = -800μA/cm²
I_pdep = -1200μA/cm² +
I_pdep = -2000μA/cm²

Figure 8

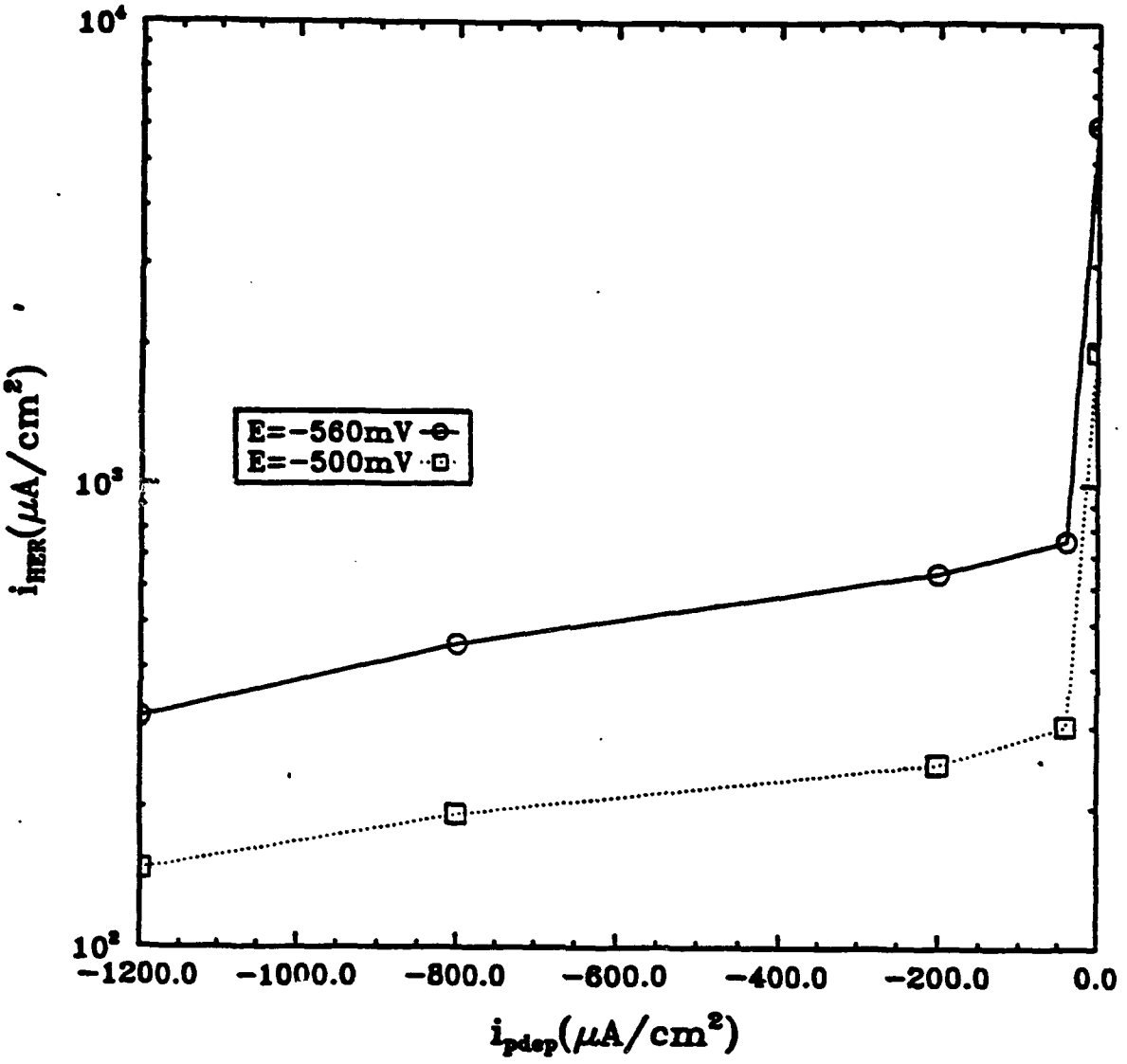
10^4
10^3
10^2
$i_{HER}(\mu A/cm^2)$
E=-560mV
E=-500mV
-1200.0
-1000.0
-800.0
-600.0
-400.0
-200.0
0.0
$i_{pdep}(\mu A/cm^2)$

Figure 9

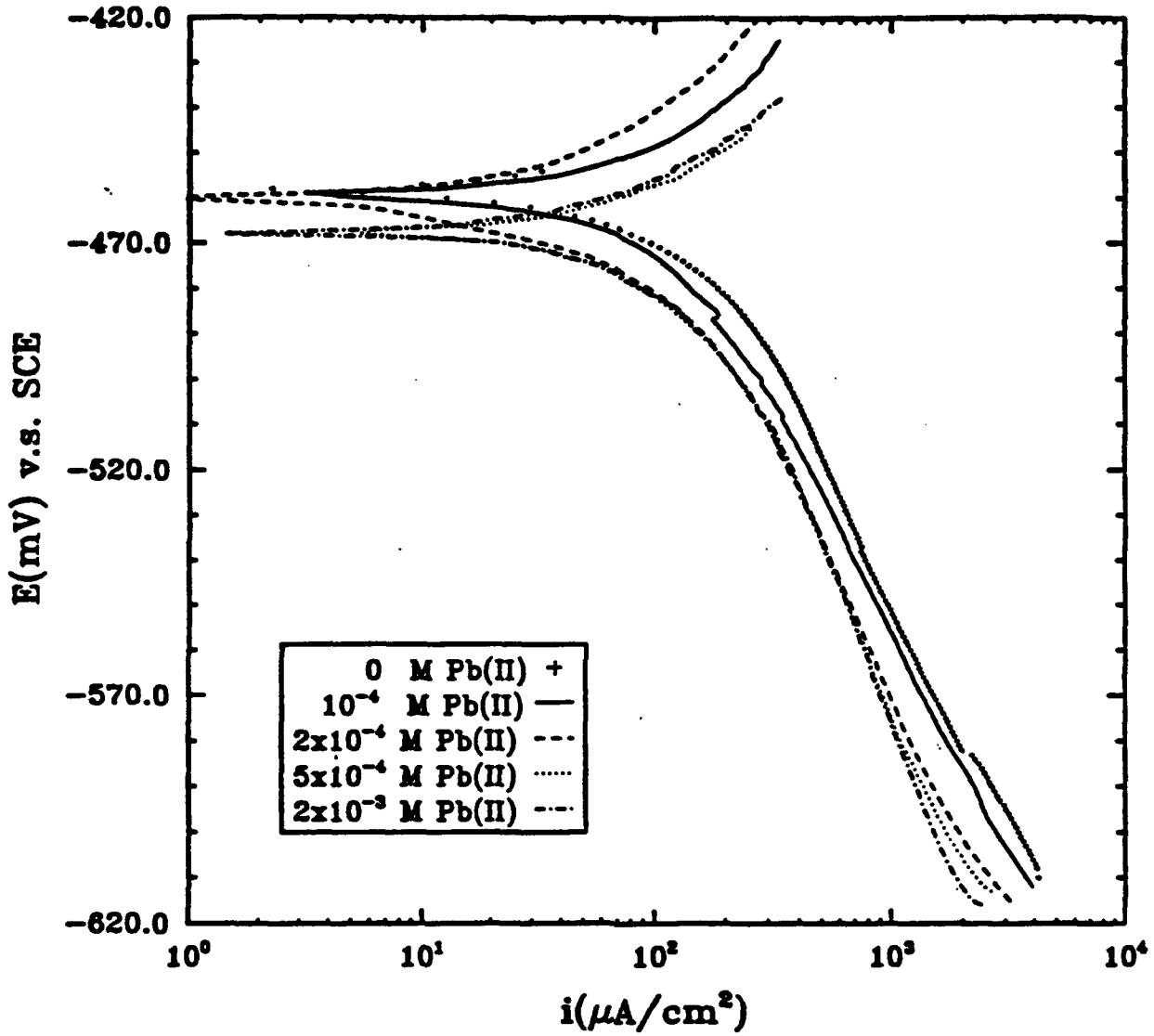
-420.0
-470.0
-520.0
-570.0
-620.0
E(mV) v.s. SCE
10^0
10^1
10^2
10^3
10^4
i(μA/cm^2)
0 M Pb(II) +
10^-4 M Pb(II) —
2x10^-4 M Pb(II) ---
5x10^-4 M Pb(II) .....
2x10^-3 M Pb(II) -·-·

Figure 10

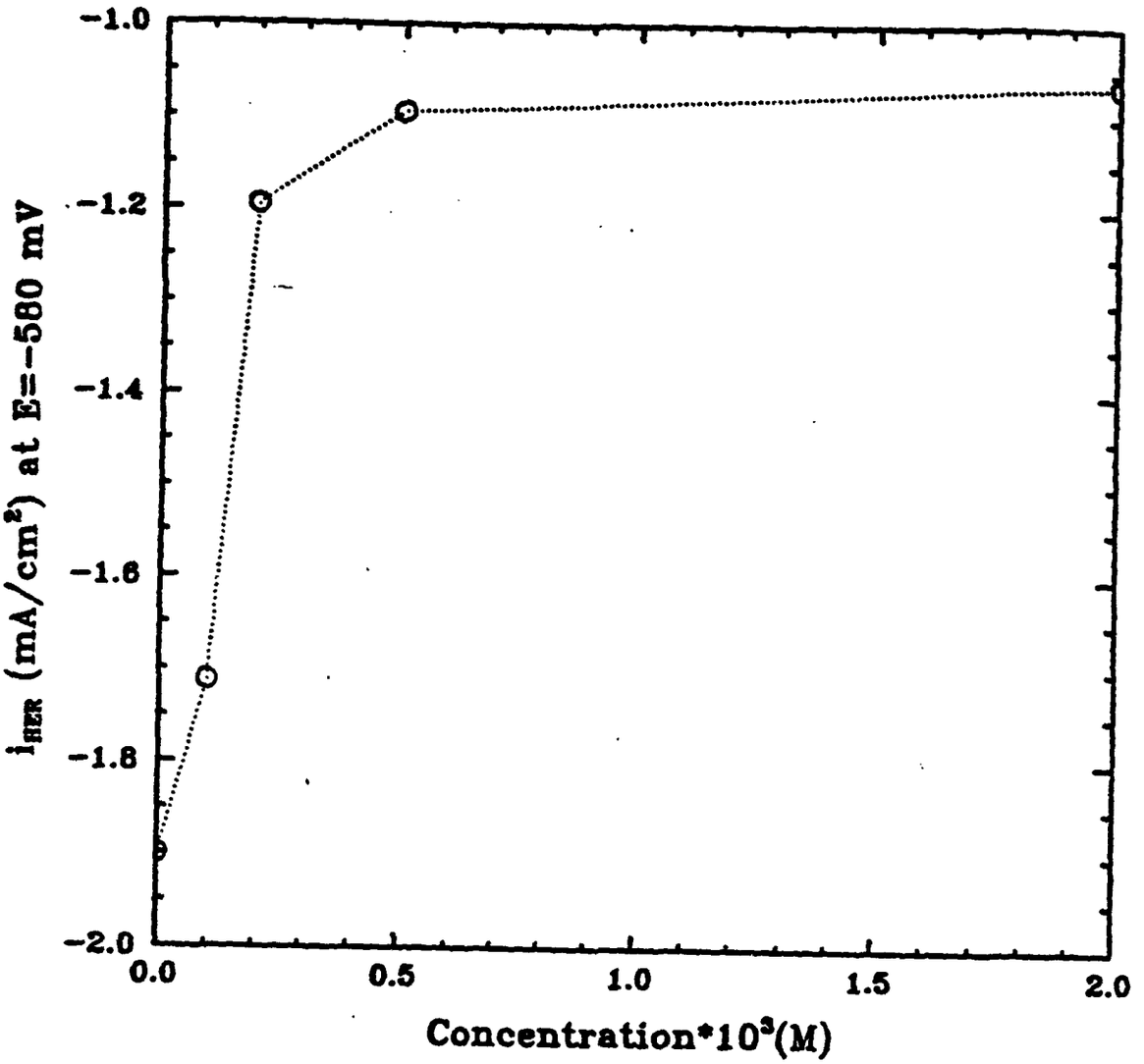
-1.0
-1.2
-1.4
-1.6
-1.8
-2.0
i_{HER} (mA/cm^2) at E=-580 mV
0.0
0.5
1.0
1.5
2.0
Concentration*10^3(M)

Figure 11

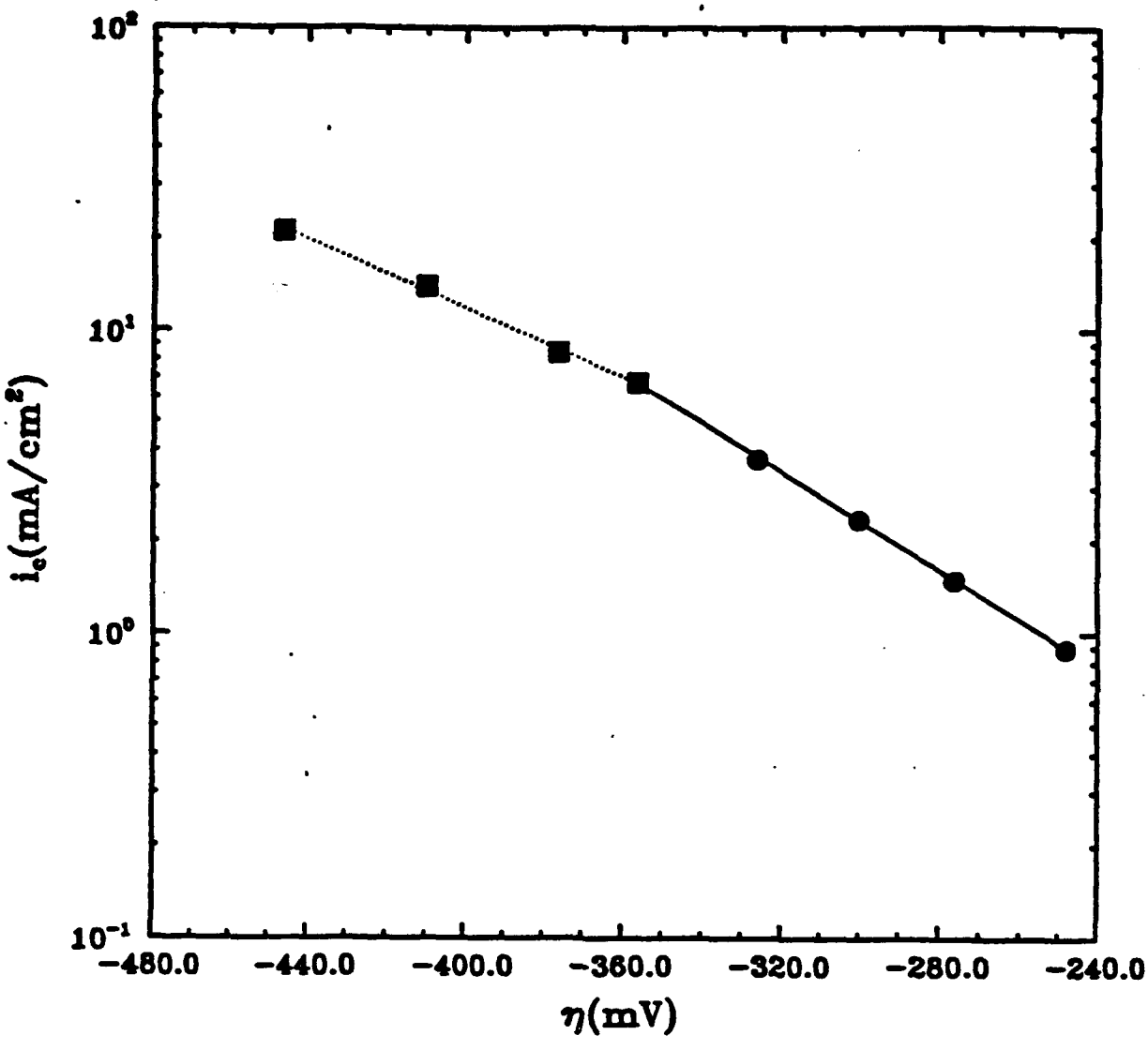
10^2
10^1
10^0
10^{-1}
i_c(mA/cm^2)
-480.0
-440.0
-400.0
-360.0
-320.0
-280.0
-240.0
η(mV)

Figure 12

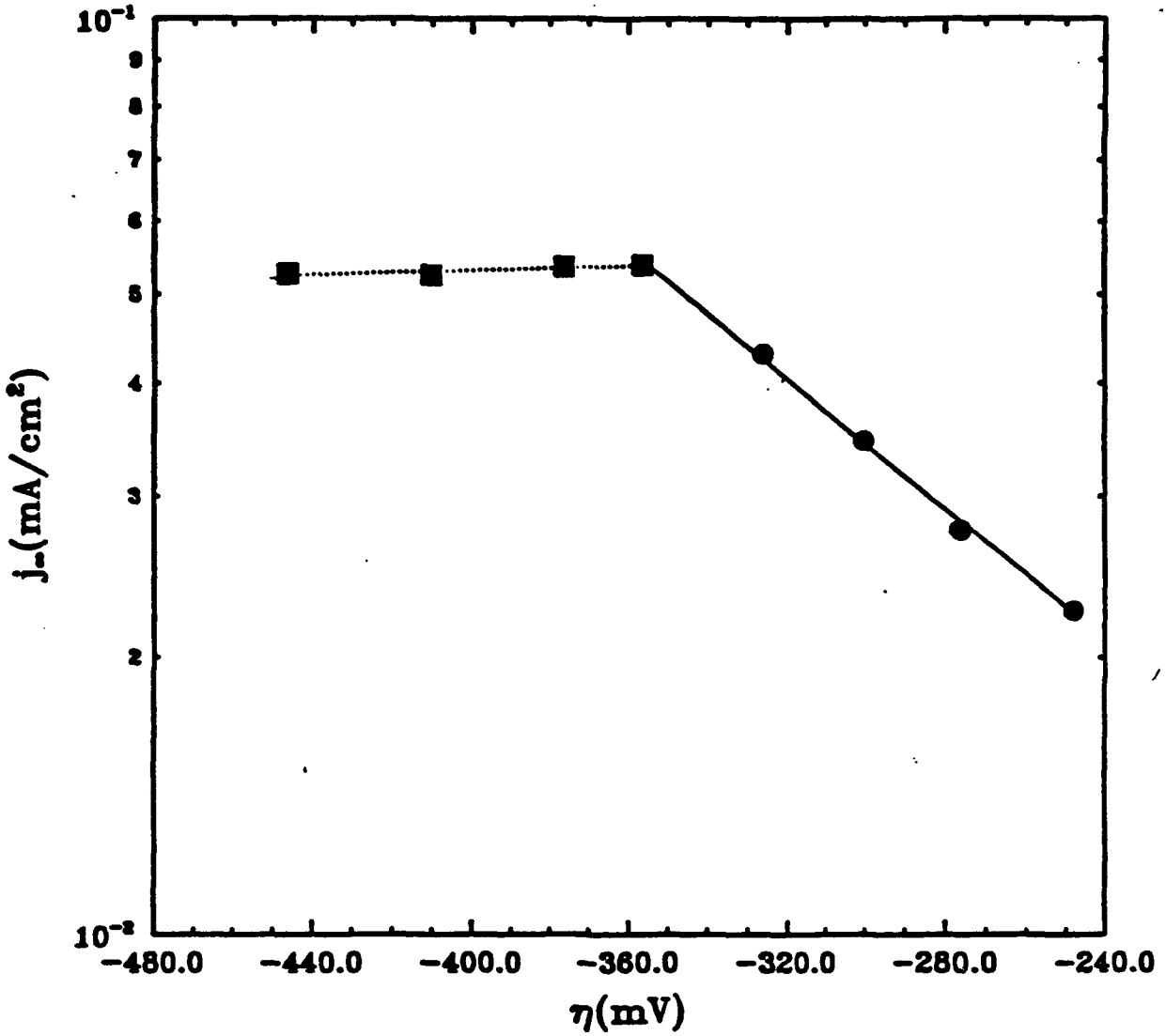
10^{-1}
9
8
7
6
5
4
3
2
10^{-2}
j_c(mA/cm^2)
−480.0
−440.0
−400.0
−360.0
−320.0
−280.0
−240.0
η(mV)

Figure 13

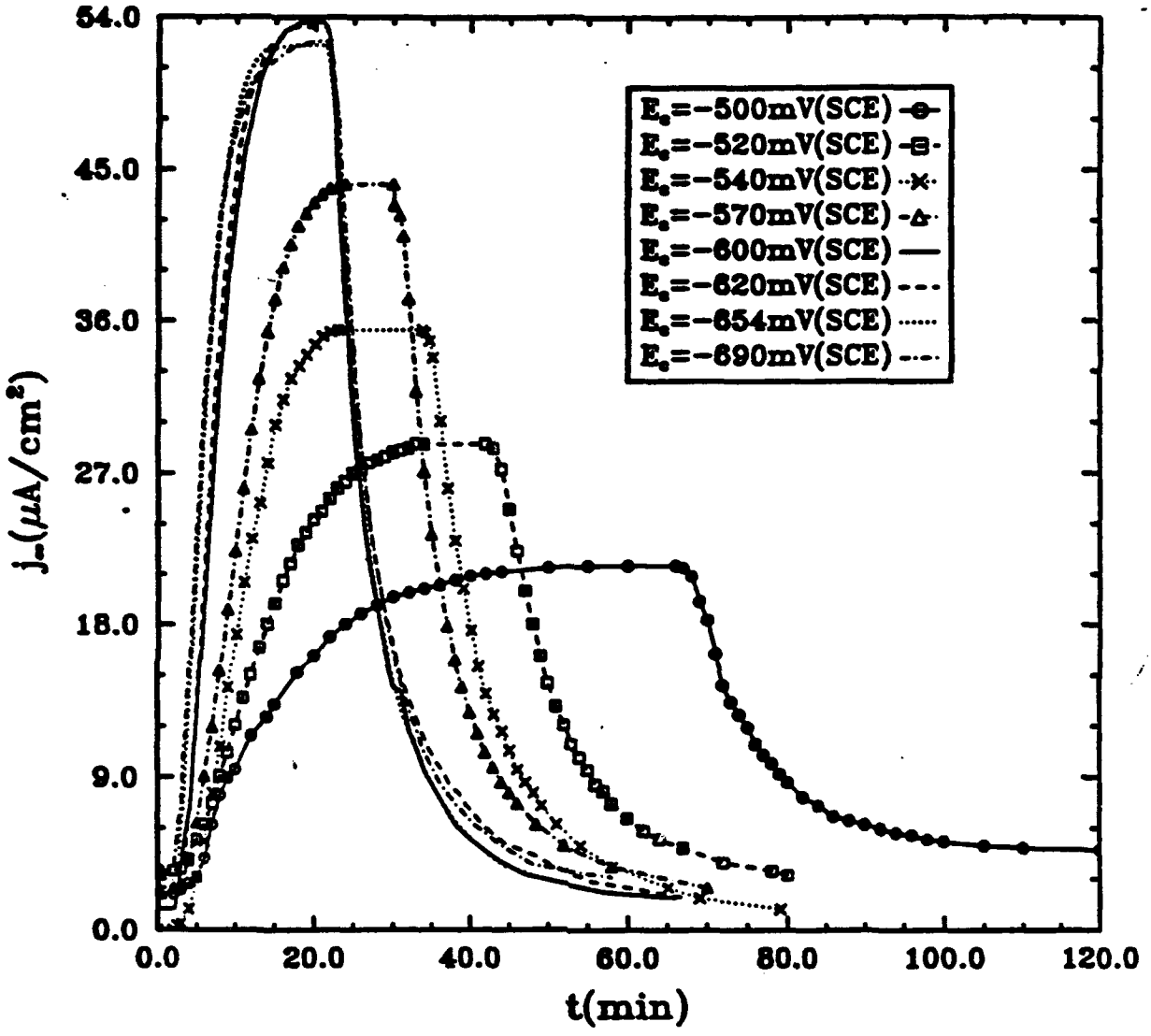
54.0
45.0
36.0
27.0
18.0
9.0
0.0
0.0
20.0
40.0
60.0
80.0
100.0
120.0
t(min)
j(μA/cm²)
E=-500mV(SCE)
E=-520mV(SCE)
E=-540mV(SCE)
E=-570mV(SCE)
E=-600mV(SCE)
E=-620mV(SCE)
E=-654mV(SCE)
E=-690mV(SCE)

Figure 14

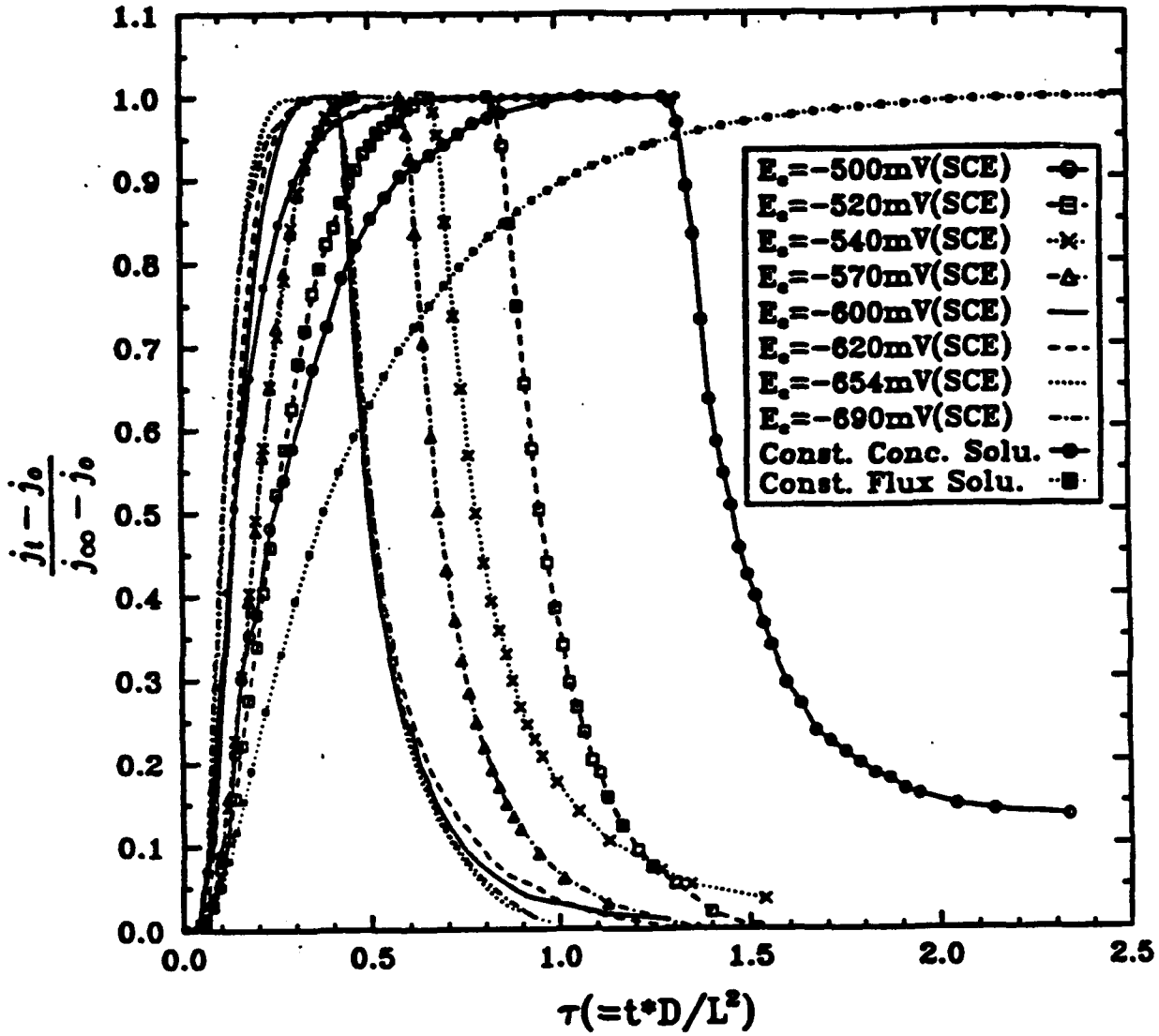
1.1
1.0
0.9
0.8
0.7
0.6
0.5
0.4
0.3
0.2
0.1
0.0
0.0
0.5
1.0
1.5
2.0
2.5
$\frac{j_t - j_o}{j_\infty - j_o}$
$\tau(=t^*D/L^2)$
E_e=-500mV(SCE)
E_e=-520mV(SCE)
E_e=-540mV(SCE)
E_e=-570mV(SCE)
E_e=-600mV(SCE)
E_e=-620mV(SCE)
E_e=-654mV(SCE)
E_e=-690mV(SCE)
Const. Conc. Solu.
Const. Flux Solu.

Figure 15

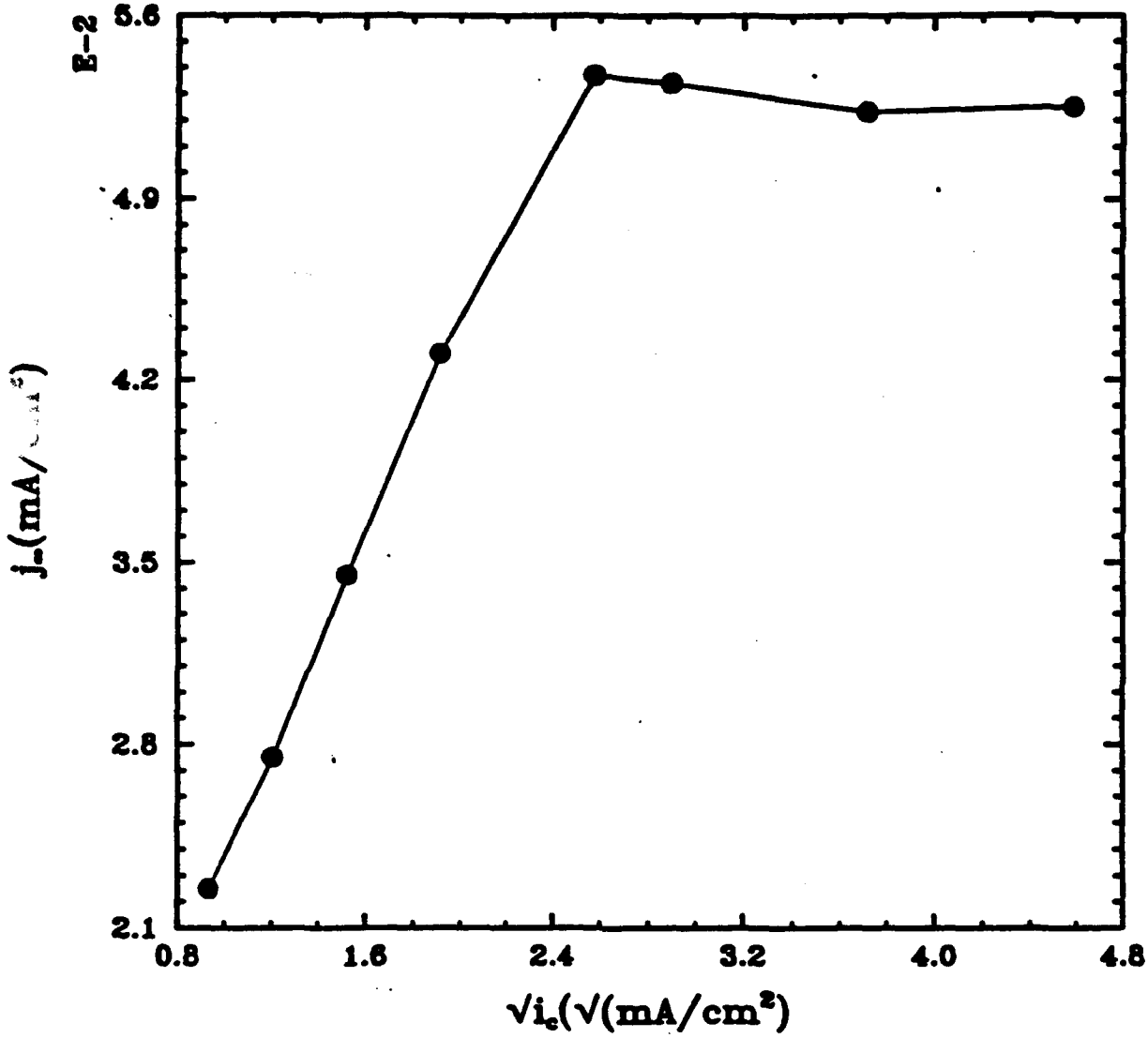

Figure 16

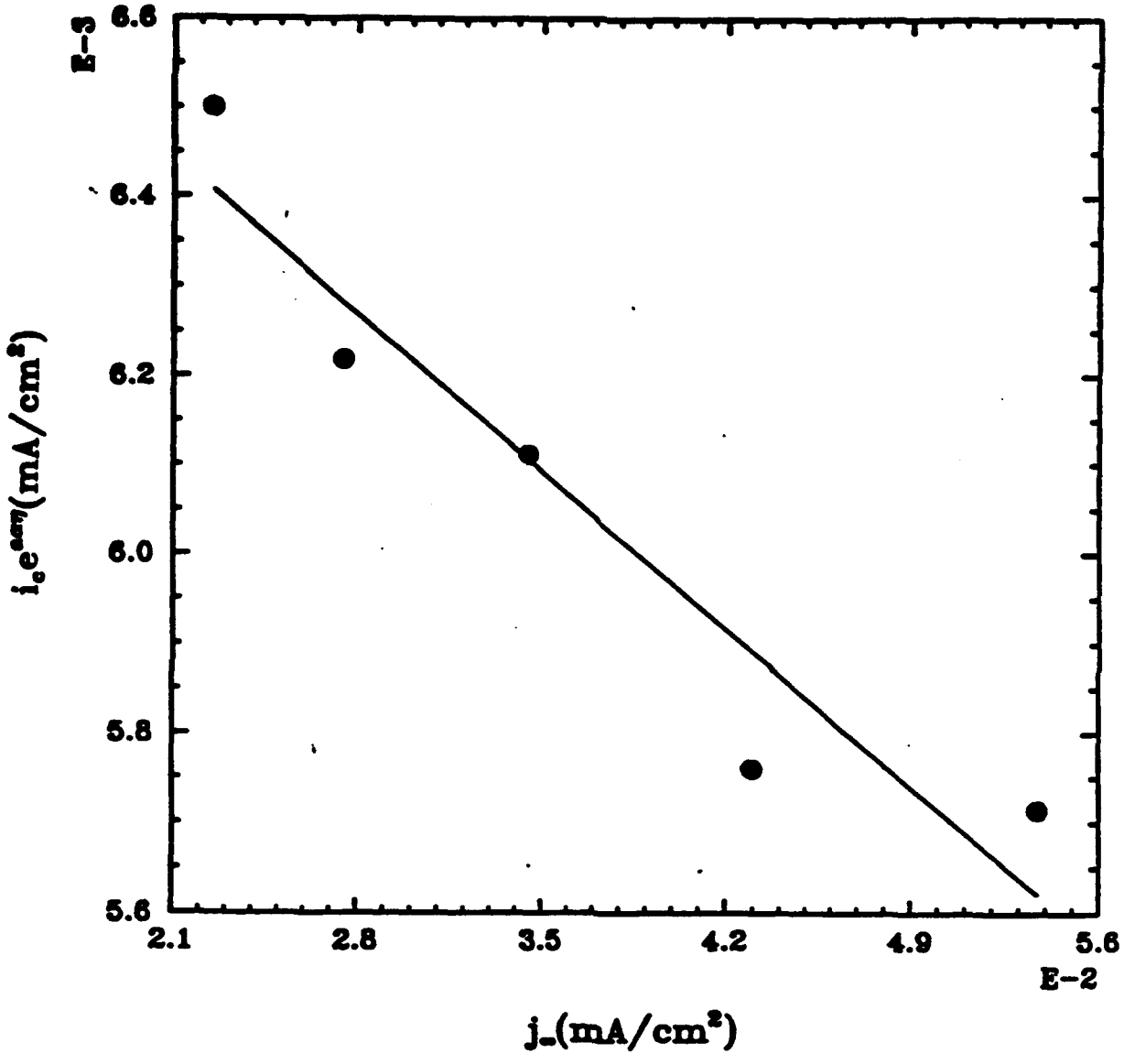

Figure 17

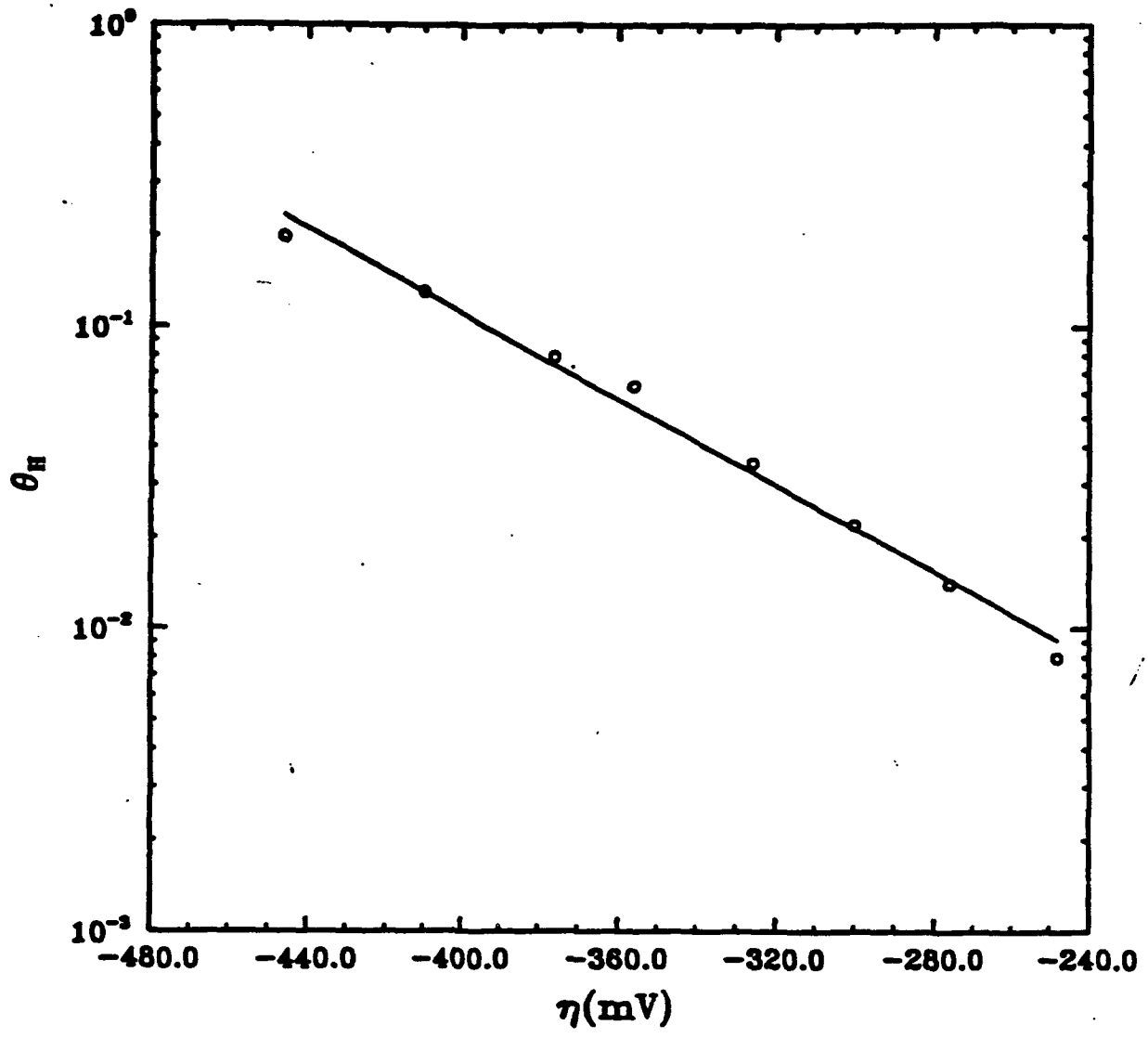
10^{0}
10^{-1}
10^{-2}
10^{-3}
θ_H
−480.0
−440.0
−400.0
−360.0
−320.0
−280.0
−240.0
η(mV)

Figure 18

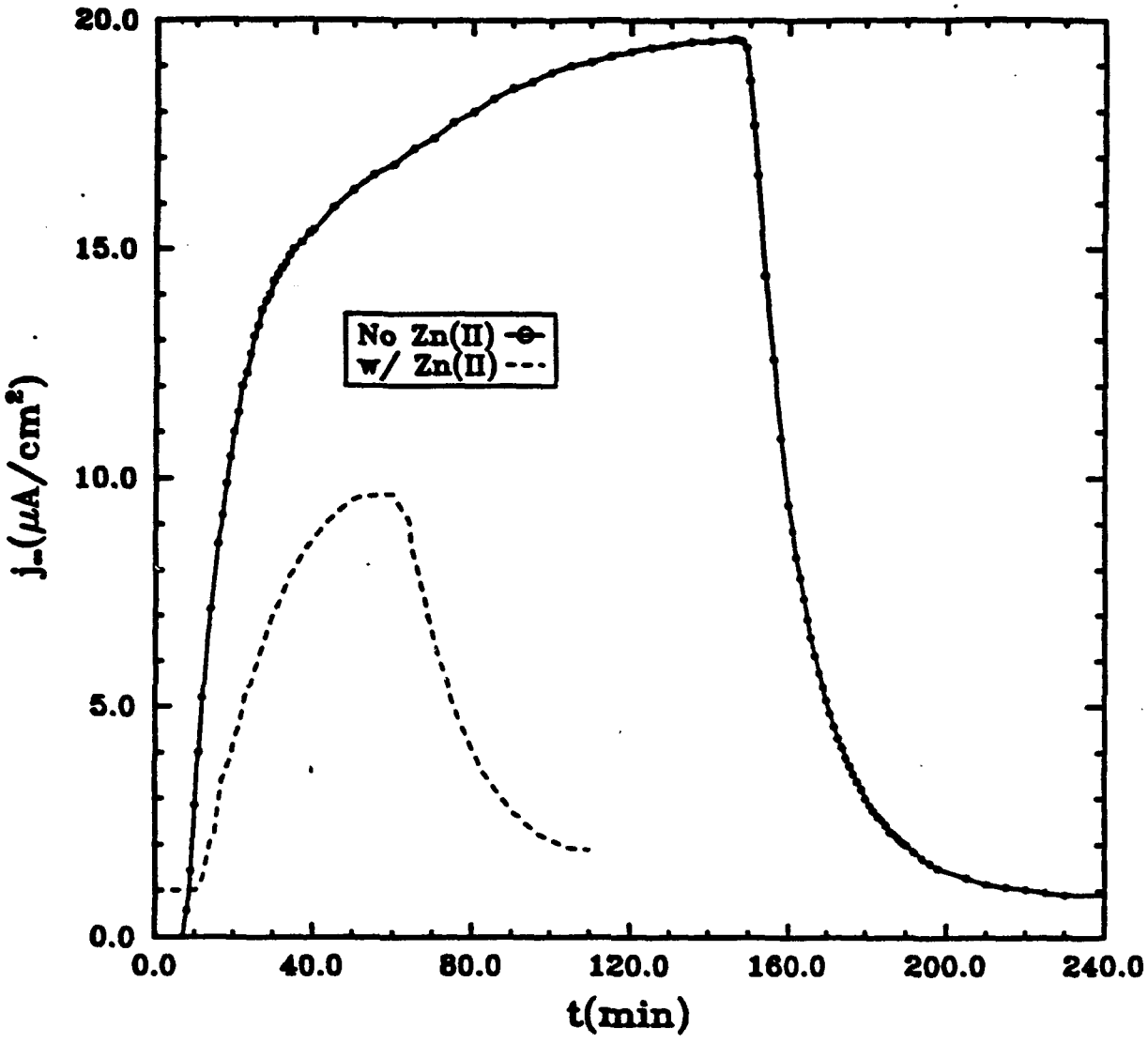
20.0
15.0
10.0
5.0
0.0
0.0
40.0
80.0
120.0
160.0
200.0
240.0
t(min)
j-(μA/cm²)
No Zn(II)
w/ Zn(II)

Figure 19

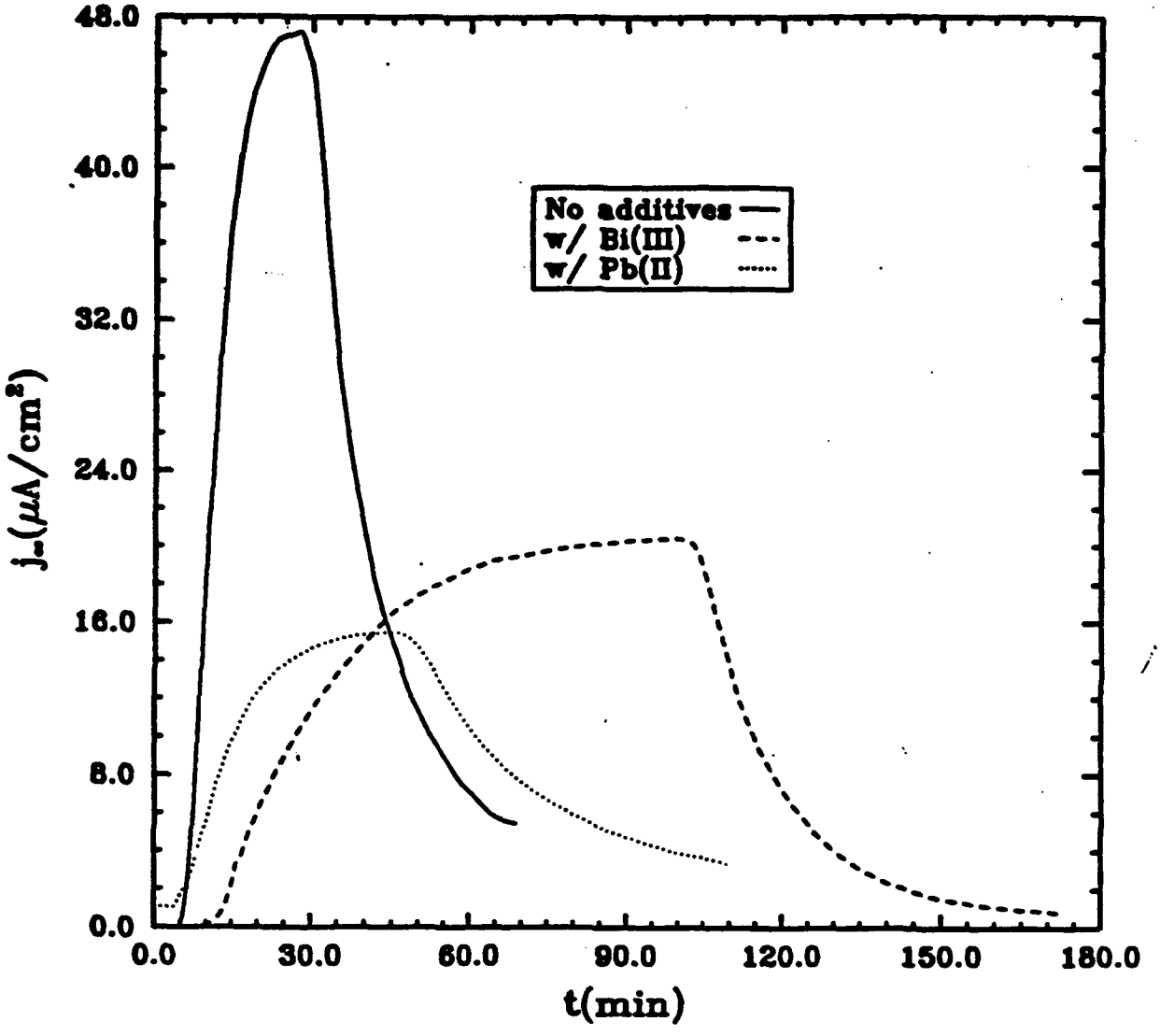
48.0
40.0
32.0
24.0
16.0
8.0
0.0
$j_a(\mu A/cm^2)$
No additives
w/ Bi(III)
w/ Pb(II)
0.0
30.0
60.0
90.0
120.0
150.0
180.0
t(min)

Figure 20